Integration of Physically-based and Data-driven Approaches for Thermal Field Prediction in Additive Manufacturing

Jingran Li

Thesis submitted to the faculty of the Virginia Polytechnic Institute and State University in partial fulfillment of the requirements for the degree of

Master of Science

In

Materials Science and Engineering

Hang Yu, Chair

Ran Jin

Rakesh Kapania

September 22nd, 2017

Blacksburg, Virginia

Keywords: additive manufacturing, geometry of freeform, layer-to-layer modeling, numerical simulation

Integration of Physically-based and Data-driven Approaches for Thermal Field Prediction in Additive Manufacturing

Jingran Li

ABSTRACT

A quantitative understanding of thermal field evolution is vital for quality control in additive manufacturing (AM). Because of the unknown material parameters, high computational costs, and imperfect understanding of the underlying science, physically-based approaches alone are insufficient for component-scale thermal field prediction. Here, I present a new framework that integrates physically-based and data-driven approaches with quasi in situ thermal imaging to address this problem. The framework consists of (i) thermal modeling using 3D finite element analysis (FEA), (ii) surrogate modeling using functional Gaussian process, and (iii) Bayesian calibration using the thermal imaging data. Based on heat transfer laws, I first investigate the transient thermal behavior during AM using 3D FEA. A functional Gaussian process-based surrogate model is then constructed to reduce the computational costs from the high-fidelity, physically-based model. I finally employ a Bayesian calibration method, which incorporates the surrogate model and thermal measurements, to enable layer-to-layer thermal field prediction across the whole component. A case study on fused deposition modeling is conducted for components with 7 to 16 layers. The cross-validation results show that the proposed framework allows for accurate and fast thermal field prediction for components with different process settings and geometric designs.

Integration of Physically-based and Data-driven Approaches for Thermal Field Prediction in Additive Manufacturing

Jingran Li

GENERAL AUDIENCE ABSTRACT

This paper aims to achieve the layer to layer temperature monitoring and consequently predict the temperature distribution for any new freeform geometry. An engineering statistical synergistic model is proposed to integrate the pure statistical methods and finite element modeling (FEM), which is physically meaningful as well as accurate for temperature prediction. Besides, this proposed synergistic model contains geometry information, which can be applied to any freeform geometry. This paper serves to enable a holistic cyber physical systems-based approach for the additive manufacturing (AM) not only restricted in fused deposition modeling (FDM) process but also can be extended to powder-based process like laser engineered net shaping (LENS) and selective laser sintering (SLS). This paper as well as the scheduled future works will make it affordable for customized AM including customized geometries and materials, which will greatly accelerate the transition from rapid prototyping to rapid manufacturing. This article demonstrates a first evaluation of engineering statistical synergistic model in AM technology, which gives a perspective on future researches about online quality monitoring and control of AM based data fusion principles.

ACKNOWLEDGEMENTS

I would like to thank my advisor, Dr. Hang Yu, for his guidance and mentoring throughout my research. I really appreciate his concern about the quality of my work. I would also like to thank my advisor, Dr. Ran Jin, for his rigorous research attitude and concern about my academic and professional goals. I would also like to thank my committee member, Dr. Rakesh Kapania, for his kind advice. I would also like to thank Mr. David Garcia for his assistance in collecting the 3D laser scanning data. I would also like to thank Miss. Lijie Ge for her assistance in collecting the microscopic images of the printed parts. I would also like to thank all my colleagues in Data Science and Visualization Lab for their kind help about 3D printing and thermal image capturing. I would also like to thank the entire Materials Science and Engineering department staff for their administrative support. Last, but not least, I would like to thank my love and family for their support, patience, and confidence.

Table of Contents

List of Figures

List of Tables

Chapter 1: Introduction

Additive Manufacturing (AM), also referred to as rapid prototyping, solid freeform fabrication, and three dimensional (3D) printing, fabricates 3D parts by additively fusing one layer of raw materials over the previously fused layers [1]. As an alternative to the conventional subtractive manufacturing techniques, AM has a large number of key advantages, like the elimination of molds, less material wastes [2], more complex geometrical designs [3], and mass customization. However, poor part integrity and various quality defects are among the biggest problems for AM to overcome. The defects like porosity, low surface finish, delamination, cracking, swelling, and residual stress are the major drawbacks encountered in AM processes [4-6], which will finally deteriorate the process outputs like static or dynamic mechanical properties and geometric conformity.

The physically-based modeling, like finite element analysis (FEA) simulation, has been applied to simulate thermal field evolution as well as calculating the local cooling rates[7] in AM. The physically-based modeling can help understand the manufacturing system through engineering knowledge, but always time consuming. Therefore, statistical methods are necessary to help capture the unavoidable model discrepancy in a timely efficient way.

The goal of this research is to have a quantitative understanding of thermal field evolution, which is vital for quality control in AM. To achieve this goal, I propose a new framework integrating physically-based and data-driven approaches for component-scale, layer-to-layer thermal field prediction in AM. The physically-based (i.e. thermal modeling) and data-driven (i.e. surrogate model using functional Gaussian process) approaches are integrated to link the process inputs to the thermal field evolution, involving using the thermal imaging data for Bayesian calibration [8]. Assisted by statistical inferences and informed by experimental measurements, this framework enables fast, accurate prediction of the thermal field evolution under different AM process conditions and with new component geometries. As a proof of concept, I demonstrate this framework using fused deposition modeling (FDM) of polymers; I expect this framework to be effective for other AM processes, such as directed energy deposition or powder bed fusion of metals.

Chapter 2: Review of Literature

2.1 Additive Manufacturing

Additive Manufacturing (AM), also referred to as rapid prototyping, solid freeform fabrication, and three dimensional (3D) printing, fabricates 3D parts by additively fusing one layer of raw materials over the previously fused layers [1]. Different in the way layers are deposited and in the used material types, there are a large number of AM processes available nowadays. In general, as illustrated in [9], the AM processes can be classified into the following aspects: laser-based processes, extrusion-based processes, material jetting processes, adhesive-based processes, electron beam processes. In the laser-based processes, a laser source is applied to melt, solidify or cure the material. Based on the phase change mechanism, the laser-based processes can be grouped into two sub-categories: laser melting [10], where the powders are melt by a laser beam; and laser polymerization [11], where the material is a photosensitive resin. In the extrusion-based processes, a heated extrusion nozzle is used to soften plastic material, including two typical methods: FDM process [12], which applies a moveable head to deposit a thread of molten thermoplastic material onto a substrate; and robocasting processes [13], which is a layer-wise deposition for colloidal slurries freeform fabrication technology. In the material jetting processes, an adhesive binder is used to bind the powder in a solid object, which includes inkjet printing processes [14], multijet modeling [15], ballistic particle manufacturing [16]. In the adhesive-based processes, which is of limited use currently, a thin film of plastic is cut and then pressed down onto the previous one by a heated compactor. Laminated object manufacturing [17] and solid foil polymerization [18] are two typical processes in the adhesive-based processes. Similar to the laser-melting processes, electron beam processes [19] melt or sinter the material by an electron beam instead of a laser beam.

As an alternative to the conventional subtractive manufacturing techniques, AM has a large number of key advantages, like the elimination of molds, less material wastes [2], more complex geometrical designs [3], and mass customization. However, poor part integrity and various quality defects are among the biggest problems for AM to overcome. The defects like porosity, low surface finish, delamination, cracking, swelling, and residual stress are the major drawbacks encountered

in AM processes [4-6], which will finally deteriorate the process outputs like static or dynamic mechanical properties and geometric conformity. In order to achieve better product quality, the most significant task is to figure out what process parameters are related to build quality and what defects can be resulted in by these improper process parameters. As illustrated in the process mapping flowchart in [20], the significant process inputs include AM machine settings, part geometrical designs, build environment factors, and feedstock qualities. There have been numerous researches on the influence of AM machine settings like laser printing strategies [21], laser power, speed, spot diameter [22], powder layer thickness, preheat temperature [23], and hatching spacing [24] [25] on part quality as summarized in [26].

Similar to those traditional manufacturing methods, like casting and welding, porosity is a common issue in AM processes which can seriously influence the mechanical properties [20]. Porosity can be classified into two groups as powder induced and process-induced [27], where the powder induced porosity is directly translated from gas pores inside the powder feedstock while the process induced porosity results from unsuitable process parameters. Some techniques like hot isostatic pressing and double melt method [28] were proposed to eliminate the feedstock internal porosity and furtherly to reduce the powder induced porosity in the final parts [29, 30]. Compared with the powder induced porosity, the process induced one has received more research attention since it can be eliminated by tuning the process parameters properly. The high viscosity [31] and the solubility decrease [32] of molten powder materials, improper laser scanning strategies [21], laser power, speed [33], spot diameter, powder layer thickness, preheat temperature [23], hatching spacing [24] would detrimentally cause porosity since low energy input would decrease the area of melt pool and lead to incomplete consolidation [25]. The porosity will continuously have influence on surface roughness and finally geometrical accuracy [20, 31, 34-36]. Cracking is also a common defect generated in AM processes, which can be grouped into microscopic cracks and macroscopic ones. Among the microscopic cracks, solidification cracking often occurs in the case when the high applied energy causes the high thermal gradients, as well as the large thermal stress on the melt pool [37]. Another type of microscopic cracking called grain boundary cracking nucleates along material grain boundaries, which depends on the formation of precipitate phases and the grain boundary morphology [37]. Macroscopic cracks are different from microscopic ones, which may relate to defects like delamination caused by incomplete melting between layers [38].

Swelling is another type of defect, where the solid materials rise above powder distribution plane due to the melt pool surface tension effects [27]. Besides swelling, surface tension is also the driver for melt ball formation [39]. Residual stresses are always introduced in AM parts by large thermal gradients during processing, which can have seriously negative impact on mechanical properties [40]. In powder bed fusion (PBF) and direct energy deposition (DED) parts, the residual stresses are always compressive in the center and tensile at the edge [41-44]. Some researchers have been conducted to relieve the residual stresses, like preheating the substrate [40] and applying island scanning [45, 46].

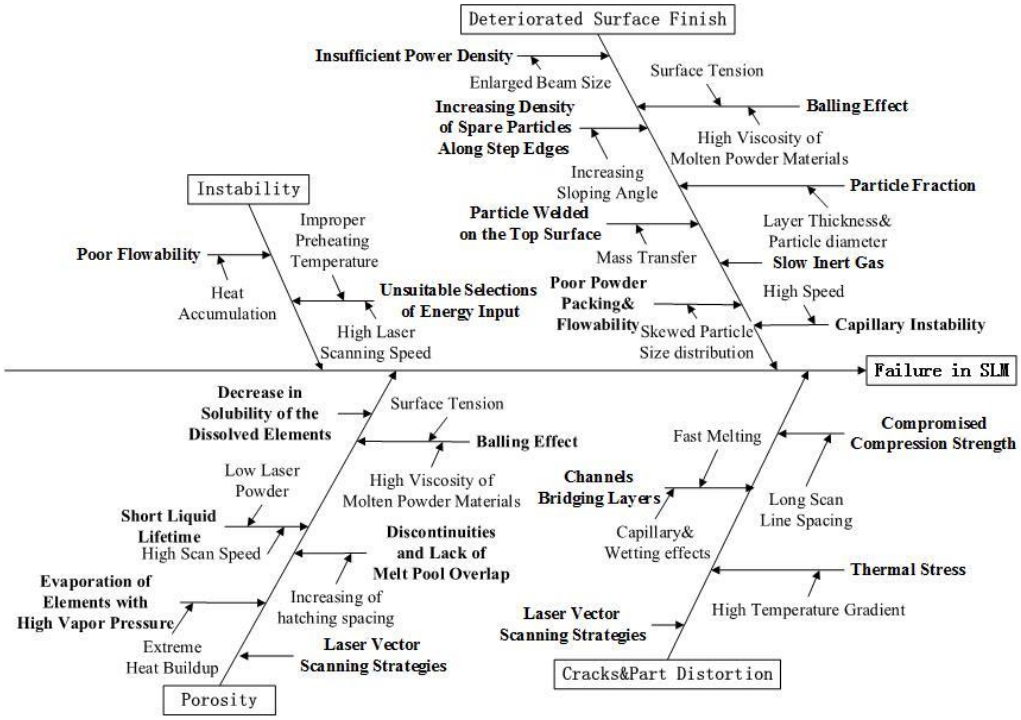

Figure 1. Fish bone graph of root causes related to SLM defects.

In this research, the FDM in AM processes is mainly studied. FDM is a process of layer to layer deposition of extruded material through a nozzle using feedstock filaments from a spool [47], which is an alternative to the conventional manufacturing techniques that enables the direct fabrication of products with complex shapes. FDM process involves heat and mass transfer, thermos-mechanical field and phase changes, which will often has deviations from the design specifications. Thus, low dimensional accuracy and poor part mechanical properties seriously limit the wide commercial application of FDM process.

2.2 Finite Element Analysis

As summarized in [26], the part microstructure, distortion, and mechanical property are all related to thermal field evolution, which shows the importance of understanding the transient heat transfer associated with AM processes [48]. The physically-based modeling, like finite element analysis (FEA) simulation, has been applied to simulate thermal field evolution as well as calculating the local cooling rates[7]. The previous thermal field simulation researches mainly focused on the 1D model like a single track [49, 50] or the 2D model like a single layer [51-53]. Although 1D and 2D FEA models have advantages in saving computation time and illustrating the key characteristics, a 3D model can better reflect the actual AM processes by considering the interaction among layers [54]. However, the existing researches on 3D FEA simulation are typically applied to simple geometries like a three-layer component [55] or a small cuboid [48, 56]. Although a thermomechanical modeling of large parts in AM processes were investigated in [57], it was restricted to the specific component geometry, which cannot be widely applied to geometry of freeform.

FEA approach has been used to evaluate the performance of various printing process variables. Wang *et al*. [58] analyzed the essence of warp deformation of FDM part and constructed a simplified mathematical model. Beuth and Narayan researched the delamination of multi-layer depositions by FEA in [59]. Zhang and Chou [60, 61] established an FEA model using the element activation function to evaluate the stress distribution at different process parameter combinations as well as the tool path effects. No restricted in FDM process, FEA has been gradually used in laser based additive manufacturing processes. Bugeda *et al*. [62] studied the influence of different parameters on the curl distortion in stereolithography processes using FEA. Nickel *et al*. [63] conducted a 3D FEA model of shape deposition manufacturing process to find out the relationship between deposition patterns and deflections. Dai and Shaw [64-66] investigated the temperature distribution and residual stresses of a solid freeform fabrication process by developing a 3D thermomechanical FEA model.

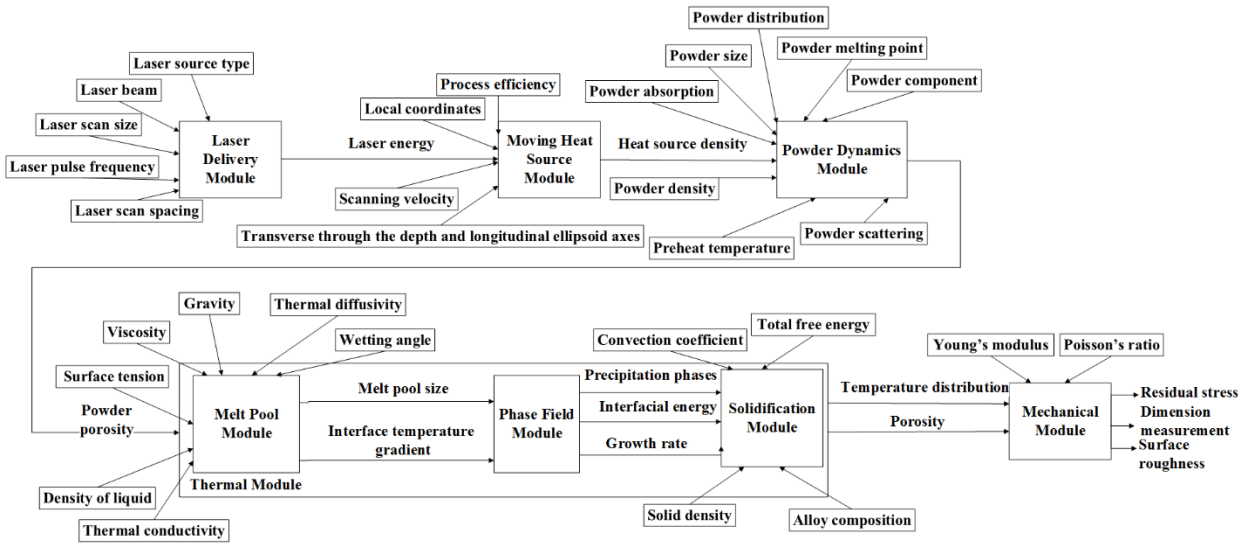

Figure 2. Finite element analysis steps in additive manufacturing processes [67-76].

Although the physically-based modeling methods like FEA can help understand the system through engineering knowledge, they are always time consuming, e.g., about 100 hours for a beam substrate with $15.2 \times 2.5 \times 0.6\, cm^3$ in FEA simulation introduced in [63]. Thus, some simplification assumptions, like not considering radiation or latent heat, are employed to speed up the computation. Besides, some parameters in the FEA simulation like heat convection coefficient [61] are hard to determine. Furtherly, both the assumptions and unsuitable selection of model parameters will lead to the model discrepancy between the FEA simulation and the actual experiments.

2.3 Sensor-based Process Monitoring in Additive Manufacturing

In laser-based systems, CMOS camera and photodiode are usually coaxially mounted to directly investigate the melt pool shape and temperature. As the laser uses the same optical path, the field of view of the observation system is always on the melt pool. Melt pool properties as area, length and width of the melt, together with the photodiode signal are obtained through the proposed sensor system. The major difference between the photodiode and the camera is the integrating effect of the photodiode (process light from larger zone around the melt is captured by the diode), while the camera can only give local information [77, 78]. Furthermore, a novel way of representing the melt pool data, namely mapping the melt pool data on the XY-plane is employed for detection of

typical processing problems during SLM [10]. Because the field of view is moving with the laser beam, this setup eliminates the necessity to simultaneously look at the whole build platform [79]. Through the correlation of the melt pool size which is obtained by the CMOS camera and the integrated signal of the photodiode, the system can adjust the laser output power according to areas of varying thermal conductivity [80]. The revised edition of the above system combines imaging sensors with an external illumination of the interaction zone and its neighborhood for high resolved pictures at high scanning velocities to capture the surface structure and the melt pool dynamics [81]. High-speed near-infrared thermal CMOS camera and a photodiode coaxial with the laser beam ensure a high quality measurement of the melt pool, while the data analysis system to translate and visualize measured sensor values in the format of interpretable process quality images [82].

In traditional polymer manufacturing process, temperature measurements like Infrared (IR) thermography and fluorescent has been widely investigated and used. Golzar *et al*. proposed to use IR camera to measure online temperature and estimate filament diameter in fiber melt spinning process [83]. Marla *et al*. employed IR camera to measure the temperature of polymer filaments held in a stream of hot air [84, 85]. Bur *et al.* proposed to use a temperature-sensitive fluorescent dye to measure temperature profiles during extrusion of polycarbonate [86, 87]. In FDM process, there have been some researches related to online temperature measurements by thermocouple and IR camera. Rao *et al*. applied multiple sensors including 4 thermocouples on build table and 1 near extruder head to realize online quality monitoring [88]. Sun *et al*. embedded the thermocouple in the platform to measure the temperature profile and furtherly investigate the bonding between polymer layers [89]. Two thermocouples were placed with 90° degree on the build plate to estimate cooling rate [90]. Dinwiddie *et al*. proposed an online temperature monitoring system with two IR cameras, where the extended range camera captured the view of whole build part while the lightweight one mounted on the liquefier heat collected the small view of extrusion tip [91]. Seppala and Migler were interested in the cooling rate near newly extruded region and investigated the weld zone properties through side view IR thermography [92]. As summarized in [93], one of the key advantages in applying pyrometry is to collect temperature without physical contact, which makes it possible to monitor surfaces of any geometry. Besides, another important advantage is to minimize the potential degradation of the sensor. Thus, compared with low-cost thermocouple,

pyrometer or IR camera is more attractive for researchers to monitor the AM processes. Apart from the sensors used to measure temperature distribution, displacement sensors (distance sensors or proximity sensors) can also be applied to detect the presence of objects [94]. These sensors are widely used in direct energy deposition processes to monitor the layer height during the build. In this work, I choose to apply IR thermography to measure the temperature distribution of every layer under different printing process and geometries. Different from the previous researches, I try to get the top view of the temperature distribution rather than the side view. Besides, I focus on the temperature evolution along the printing path instead of the simple location.

2.4 Statistical Methods

To improve the part quality and decrease the mechanical defects, various statistical designs of experiments techniques are applied to optimize process parameters. The Taguchi's design matrix, signal to noise ratio (S/N), and analysis of variance (ANOVA) were used by Anitha *et al*. [95] to figure out that road width, deposition speed, and layer thickness are the important process parameters on ABS part surface roughness. The similar conclusion was also obtained by Nancharaiah *et al*. [96] through Taguchi and ANOVA methods. Besides, Thrimurthulu *et al*. [97] predict the optimum build orientation through an analytical model developed by genetic algorithm. Horvath *et al*. [98] and Wang *et al*. [99] also pointed that layer thickness and part fill style were the most process parameters to improve the surface roughness by factorial design and the integration of Taguchi method with the Gray relational analysis individually. Sood *et al*. [100] used artificial neural network (ANN) and fuzzy logic to predict the shrinkage along the length, width and diameter. Bansal [101] studied the effect of process parameters on dimension accuracy via Response surface methodology.

As introduced in Section 2.2, a physically-based model can take several days to simulate the thermal field of FDM process. Therefore, design optimization or sensitivity analysis would become impossible because they need thousands of simulation evaluations. Thus, a surrogate model (also known as meta-model, kriging, or emulator) [102, 103] is established using the historical data sets of the FEA simulation results. The surrogate model can mimic the results of the simulation model in a computationally cheaper way. When building the surrogate model, the underlying physics of the simulation model is not important and it even can be assumed to be

unknown. Only the input-output relationship is significant. This method can be also called as black-box modeling [104]. Kriging [105] is the most popular method for surrogate modeling because of its good interpolating property. Nevertheless, for the model with functional response like the thermal field, kriging is not suitable since computational issues may be caused due to the high dimensionality. To overcome this challenge, Bayarri *et al.* applied wavelet decomposition on the functional data [106], Ramsay [107] and Higdon *et al*. [108] utilized principal component analysis to transform the functional data to scalars. Fang et al. [109] made use of functional linear regression model to handle the functional response. However, these methods are lack of interpolation property, which cause a gap between analysis methods for scalar and functional outputs. Liu and West [110] proposed a methodology that takes the functional variable as an additional input to the model, which extended kriging to functional response. One biggest issue of this method is that the size of the correlation matrix would become too large to calculate its inversion and determinant. To solve the computational issue, Kronecker product formulation have been applied to build the correlation matrix in [111-113]. By the Kronecker product assumption, the computation complexity is reduced to a large extent, which makes it possible to investigate for kriging model with functional responses.

In usual, the physically-based models do not represent reality because of assumptions made to simplify the complex system. To compensate the possible inaccuracy, field experiment is conducted to collect real data from the system and estimate the unknown parameters (i.e., calibration parameters) in the physically-based model. Through this calibration, the model prediction would become more realistic. To capture the discrepancy between real observation and physically-based model, Kennedy and O'Hagan [8] proposed to represent it using Gaussian process models. The further improvements for the GP modeling approach were made in [106, 114-116].

Chapter 3: Methods and Experiments

3.1 Integration of Physically-based and Data-driven Modeling

A new framework is proposed in this paper for geometry of freeform prediction in the extrusion-based AM process. In this framework, the physics-based and data-driven approaches are integrated to build a synergistic model, which can be continuously updated with comparisons to the experimental measurements through Bayesian calibration (see Figure 3). Assisted by statistical inferences and informed by experimental measurements, the final synergistic model is able to predict the temperature and stress distribution in components with new processing variables and new geometry designs.

To capture the underlying processes such as heat transfer, glass transition, and thermo-mechanical coupling, I started from physics-based modeling for extrusion-based additive manufacturing, and simulate the model using 3-D FEM method. To avoid the potentially high computational cost, a surrogate model is then established to link the model inputs, such as processing variables, to the model outs, such as temperature and stress distribution during manufacturing. In the proposed framework, the surrogate model is established by training several sets of the FEM simulation data using a statistical approach, called functional Gaussian process modeling [113]. The surrogate modeling results are then compared with experimental measurements through Bayesian calibration [8], in which the unknown parameters are determined with quantified uncertainties and the model discrepancy is identified. As it is trained and updated with the new experimental data, the synergistic model not only captures the physical processes in extrusion-based AM, but also corrects for the discrepancy associated with the physical models. Finally, the synergistic model will be validated under a different set of processing variables and with a different geometrical design. The algorithm of our proposed method is summarized in Table 1.

I investigate the effectiveness of using this framework to predict thermal field evolution during extrusion-based AM. In the rest of this chapter, I elaborate on the steps of applying the proposed framework to predict thermal field evolution.

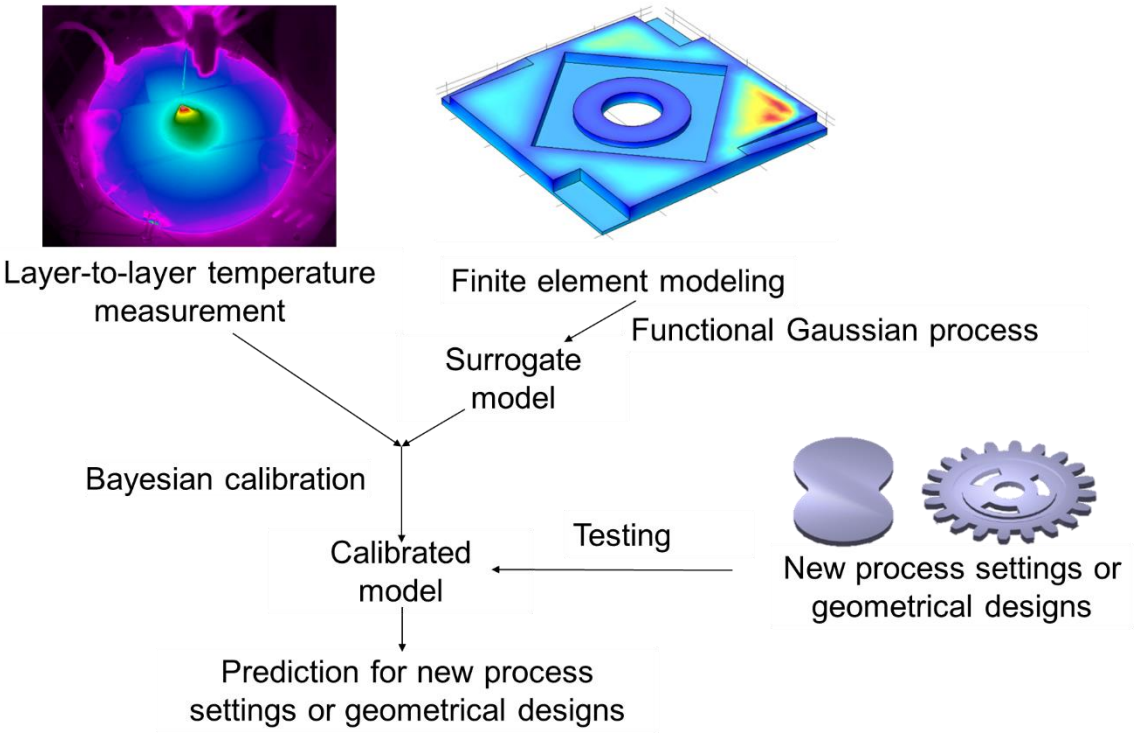

Figure 3. Illustration of the proposed framework.

Table 1. Algorithm of the engineering statistical calibrated model.

Steps	Descriptions
Step 1	Run the computer simulations.
Step 2	Establish the surrogate model for the computer simulations.
Step 3	Conduct the physical experiments.
Step 4	Integrate the physical experiments with the surrogate model to do online updating Bayesian calibration.
Step 5	Test the prediction performance of the proposed calibrated model with new input settings and new geometrical designs.

3.2 Experimental Methods

I use an open-chambered ORION DELTA™ desktop 3D printer for sample manufacturing. The filament material is semi-crystalline poly-lactic acid (PLA), with its properties listed in Table 2. All the experiments are assumed to be conducted under the fixed environment conditions. The nozzle temperature and printing speed are set according to the design of experiment (DOE) plans, ranging from $493.15{\sim}518.20\ K$ and $20{\sim}50\ mm/s$, respectively.

Table 2. Poly-lactic acid material properties.

Properties	Values
Latent heat of fusion [$\boldsymbol{J/g}$]	$10{\sim}40$
Density [$\boldsymbol{kg/m^3}$]	~ 1250
Heat capacity [$\boldsymbol{J/(kg \cdot K)}$]	~ 2020
Thermal conductivity [$\boldsymbol{W/(m \cdot K)}$]	~ 0.13

In this work, three different geometries were investigated (as shown in Figure 4): standard part (g_1), peanut part (g_2), and gear part (g_3). The size of $g_1$was $44.45 \times 44.45 \times 2.5\ mm^3$, which was revised based on the National Institute of Standards and Technology standard part [117]. It has been widely used as testing sample in additive manufacturing [88]. g_2 was of a contour function $r(\theta) = r_0(1 - sin\theta cos\theta)$, where polar angle $\theta \in [0^o, 360^o)$, polar radius $r_0 = 20\ mm$, and its height was $2\ mm$. g_3 was with the outer diameter of $55\ mm$ and the height of $2\ mm$. The number of layers in one sample varied from 7 to 16 depending on the layer thickness in the DOE plan. It took about $30\ s$ to print one layer. The three geometric contours were composed of various basic and representative contour elements like straight line, circle, sharp corner, concave curve, arc and etc.; these geometries were chosen to test the proposed method potential for any geometry of freeform.

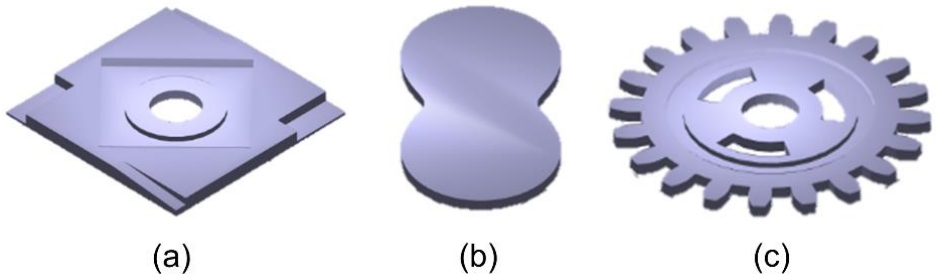

Figure 4. Three geometrical designs: (a) g_1: standard part; (b) g_2: peanut; (c) g_3: gear.

The layer-to-layer thermal images were captured by a calibrated FLIR A655sc IR camera during printing, with resolution of 640×480 pixels and frame rate of 50 Hz. Because the printing head would block the view of IR camera (Figure 5 (a)), the G-code was revised in advance to enable nozzle lifting once a layer was finished. The IR images can be captured during the printing (Figure 5 (b)) and when the nozzle is lifted (Figure 5 (c)). Although the IR camera is not set just above the printing part, image processing methods were applied to register the original IR images into the top-view format. The time delay from nozzle lifting was less than 1 s, which had been considered in both computer simulations and experiments for model calibration. As a result, this was essentially quasi in situ thermal imaging.

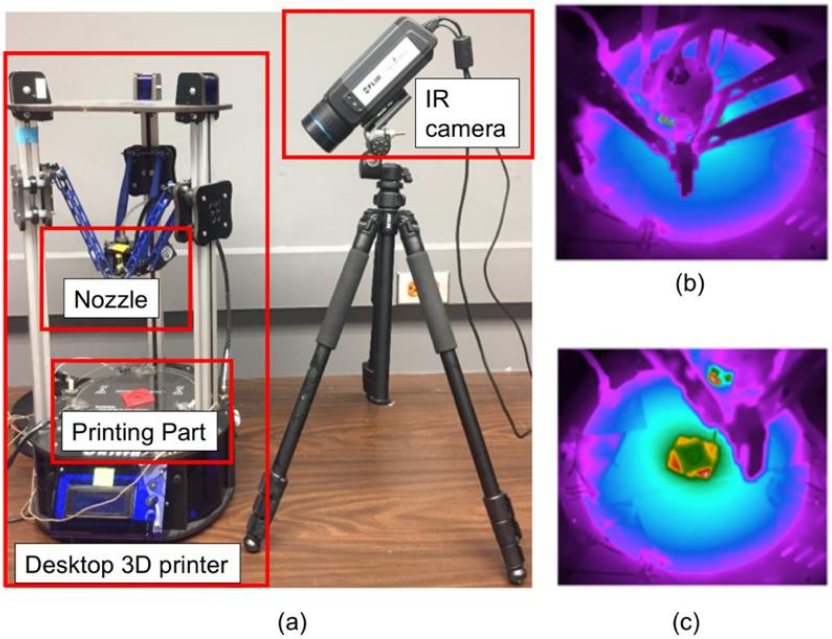

Figure 5. (a) Desktop 3D printer and IR camera setup; (b) IR image during printing; (c) IR image when the nozzle is lifted for the whole view of part.

3.3 Physically-based Modeling

3.3.1 Constitutive modeling

In FDM processes, the material filament is heated during extrusion, while the temperature of the printing table is kept constant [88]. The energy input originates from the addition of hot filament from the printing nozzle, which can be viewed as a moving heat source [60, 61]. The heat transfer during AM is mostly by heat conduction (internal and surface material voxels) and heat convection (surface material voxels).

Take g_1 part as an example, given the surface temperature as $T_{surface} \approx 400K$, the emissivity coefficient of PLA $\varepsilon_{PLA} = 0.96$, the surface area $A_{g_1} \approx 4.40 \times 10^{-3}\, m^2$, the Stefan-Boltzmann constant $\sigma = 5.6703 \times 10^{-8}\, W/m^{-2}K^{-4}$, the radiation energy per unit time can be calculated as $\varepsilon_{PLA}\sigma T_{surface}^4 A_{g_1} = 6.13\, W$, which is relatively low compared with other heat transfer mechanisms. Thus, I assume that the thermal loss by radiation can be negligible. The energy conservation equation can be given by [61]:

$$\frac{\partial(\rho C_P T)}{\partial t} = \nabla.(\kappa \nabla T) + \dot{q_V}, \tag{1}$$

where ρ is the materials density, C_P is the specific heat capacity, ∇T is the spatial gradient of the temperature, and κ is the thermal conductivity. Here, $\dot{q_V}$ is the volumetric heat generation rate caused by the addition of the heated filament, which can be modeled as a function of the printing process inputs and the material properties:

$$\dot{q_V} = Q(T_{nozzle}, v, L, \rho, C_P). \tag{2}$$

Here T_{nozzle} is the nozzle temperature, v is the printing speed, and L is the latent heat during solidification of the semi-crystalline PLA. Because the distance from the nozzle to the printing layer is short, the heat transfer from nozzle heating to filament extrusion is insignificant. Then $\dot{q_V}$ may be approximated the same as the heat input rate by nozzle heating, which can be written as

$$\dot{q_V} = \frac{\rho v[C_P(T_{nozzle} - T_{env}) + L]}{l_f}, \quad (3)$$

where T_{env} is the surrounding environment temperature and l_f is the heated filament length in the nozzle. Other treatments in modeling the volumetric heat generation rate are also found in the literature. For example, in [61, 118] the initial temperature of the newly deposited filament is assumed to be the same as the nozzle temperature. In [47, 119], the filament temperature is assumed to rise to a certain value after entering the melt flow channel. In [120], the input of material accompanied with a heat reservoir is simulated but without a specific expression. All these approximation treatments may lead to model discrepancies; possible discrepancy from the proposed treatment is expected to be corrected by the data-driven component (Section 5) in the proposed framework.

Regarding the boundary conditions, the part bottom surface is maintained at the same temperature with the printing bed $T = T_{bed}$. All the other surfaces transfer heat by convection $\dot{q_A} = h(T - T_{env})$, where $\dot{q_A}$ is the convective heat flux, and h is the natural convection heat transfer coefficient for air. Note that the glass transition temperature of the semi-crystalline PLA is about $333.15 \sim 338.15\,K$, lower than the printing bed temperature of $363.15\,K$. As a result, glass transition can only occur after the printing is finished and the printing bed heater is turned off.

3.3.2 Transient finite element analysis

With constitutive modeling, the thermal field evolution can be simulated using 3D transient FEA, in which the concept of "element activation and deactivation" [61] is employed to simulate the material addition processes. At the beginning of simulation, the meshes are constructed for both the deposited and to-be-deposited material voxels. The material properties of the deactivated elements are assigned with extremely low values, while the activated elements are applied with the regular property values. Take the part in Figure 6 (a) as an example, the values of the assigned material properties vary among the whole component during printing, where the red part corresponds to the activated elements and the blue part corresponds to the deactivated elements at a given time. Such distribution evolves as new material voxels are deposited. Since this simulation covers the whole component rather than a single layer or a single track, the elements are activated layer-by-layer to minimize the computational costs. The resultant modeling discrepancy can be

corrected by the data-driven approaches discussed in Section 3.4; this is an advantage by integrating the physical science and data science in the proposed framework. Close to the deposition region, the mesh sizes need to be fine to characterize the high temperature gradients. Nevertheless, it is unnecessary to build such high density meshes in the material voxels that are far from the nozzle (i.e. the heat source) [121]. Therefore, I use the adaptive mesh approach to make the mesh sizes adaptive to the local physical conditions [122-125] (see Figure 6 (b)).

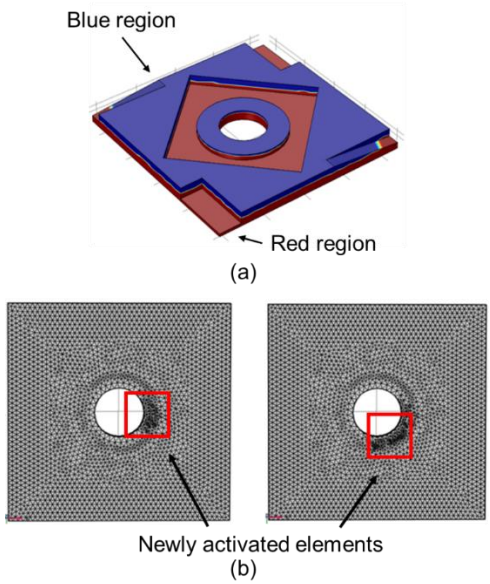

Figure 6. Use of activation and deactivation of elements, and adaptive meshes. (a) Thermal conductivity distribution during FDM of a g_1 component, where the blue and red regions correspond to the thermal conductivity values of 10^{-4} for deactivated elements and 0.13 $W/(m \cdot K)$ for activated elements, respectively. (b) Adaptive mesh refinement of the bottom surface of a g_1 component, with the interval of 10 simulation steps. The newly deposited material voxels with the finest meshes are highlighted in the red box.

Once the CAD design file and the printing process settings are given, the G-code [126] can be generated by slicing software, such as Slic3r. Both the printing paths (i.e. hatch patterns) in FEA simulations and in physical experiments are based on the generated G-code. The CAD design file, printing process settings, material information, and printing path can all be automatically loaded into the developed 3D FEA model. This significantly increases the flexibility of AM process simulations and reduces the changeover cost between different geometrical designs.

3.3.3 Representative simulation results and validation

With the high-fidelity thermal model, the "element activation and deactivation" method, and the adaptive mesh approach, the temperature distribution across the component can be computed at any given time during FDM processes. I adopt a time step size of $0.03\ s$ in the transient FEA simulation. Thus, a printing speed of $20\ mm/s$ leads to a $0.6\ mm$ spatial resolution of the G-code, which is fine compared to the size of the heat affected zone in FDM [127]. Figure 7 shows the simulation results of the temperature distribution in Layer 5 of a g1 part during FDM, using the printing speed of $44\ mm/s$, nozzle temperature of $493.15\ K$, convection coefficient of $11\ W/(m^2K)$ [128] and latent heat of $18\ J/g$ [129]. The new material voxels are being deposited at the lower-left corner. The time interval between each snapshot is $0.3s$ (10 time steps in the transient FEA model), where t refers to the time span from the beginning of the printing to the current time point. The simulation well captures the rapid cooling process near the extrusion region, with the cooling rate computed to be of the order of $100\ K/s$. This value is consistent with the previous estimation using FEA in literature [130].

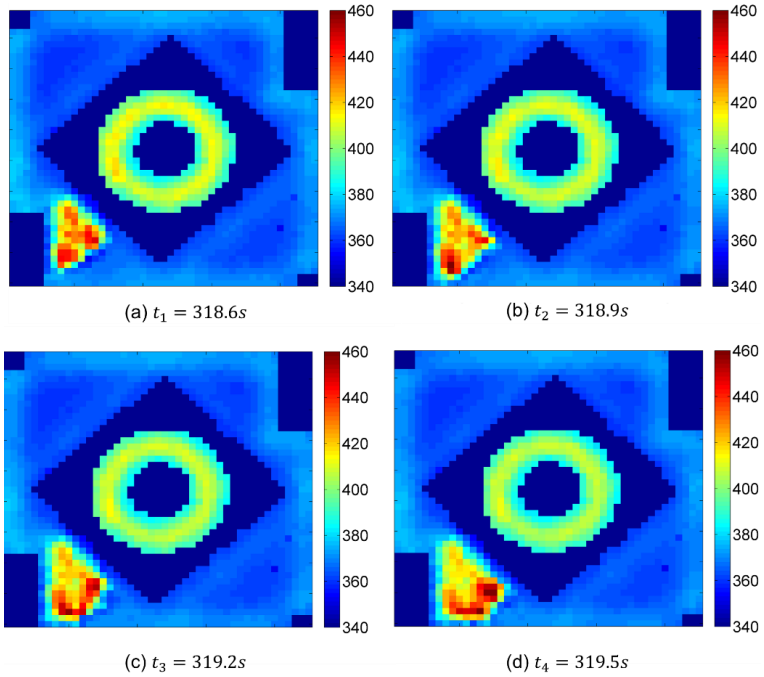

Figure 7. A representative simulation result of temperature evolution in FDM (unit: K).

The printing path of the same sample is illustrated in Figure 8 (a) and (b). The z-axis in Figure 8 (a) represents the printing sequence of every voxel. For example, the upper left corner in Figure 8 (b) has the largest z values in Figure 8 (a), which demonstrates that this corner is deposited at the latter stage of the whole printing process.

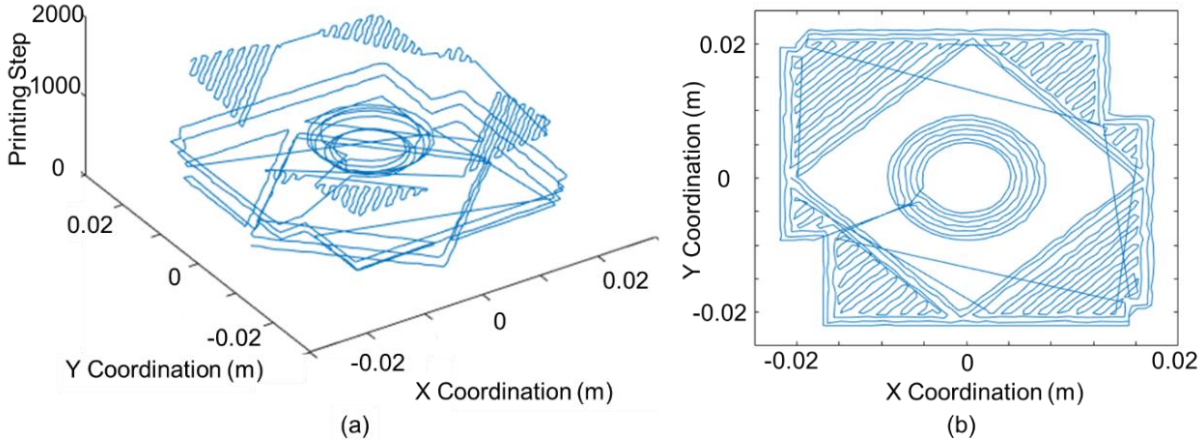

Figure 8. (a) Printing path in 3D; (b) printing path in 2D; (c) thermal field by simulation; (d) thermal field by experimental measurements (unit: K).

Take two layers from different process settings of g_1 as examples to validate the FEA model. The simulation results (Figure 9 (a, c)) are compared to the actual experimental measurements (Figure 9 (b, d)). Even with uncalibrated values of the heat convection coefficient and latent heat, the simulation leads to a temperature distribution quantitatively similar to the experimental measurements, showing the efficacy of the proposed physically-based modeling. The local deviations between the simulation and experiment suggest the importance of model calibration, which will be detailed in Section 3.4.

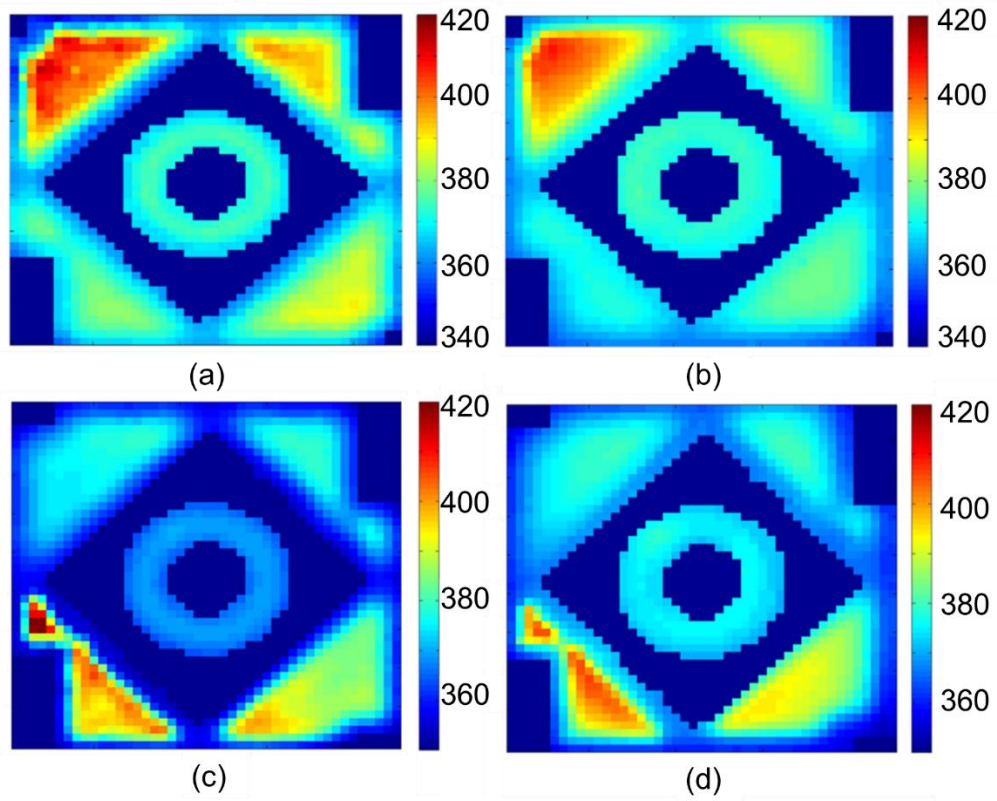

Figure 9. (a) Thermal field by simulation of g_1 part 1 layer 5 ; (b) thermal field by experimental measurements of g_1 part 1 layer 5; (c) thermal field by simulation of g_1 part 5 layer 6; (d) thermal field by experimental measurements of g_1 part 5 layer 6 (unit: K).

3.4 Data-driven Approaches

3.4.1 Surrogate Modeling

The high-fidelity, physically-based 3D FEA model, though captures the heat transfer process during the whole printing process, is computationally expensive. For a time-step of 0.03 second in the transient FEA model, the total time for simulating the temperature distribution of the whole part (g_1) is ~ 10^3 minutes using a conventional desktop computer. To reduce the computational cost, I employ a surrogate model to link the model inputs with the model outputs.

The main model output for thermal field evolution is the layer-to-layer temperature distribution. This is of a typical functional response format [131], resulting in critical challenges in surrogate modeling associated with the high computation requirements and the inadequacy of interpolation.

Here, I follow the approach proposed by Hung *et al*. [113] and use functional Gaussian process for surrogate modeling, in which the functional output responses could be solved by integrating the correlation functions from both the input setting space and the time space.

Using similar notations as those in [113], suppose that $\boldsymbol{x} = \left(x_1, \dots, x_p\right)^T$ are the p input settings (including p_1 input variables and p_2 calibration parameters) for engineering model, and the time index is t, over which functional responses $\boldsymbol{f}$ are collected. For the purpose of reducing computation cost, only regular grid situation is considered, which assumes that the functional response for every run are in the same length regardless of layer index or geometry type. Thus, the functional kriging model for computer model can be given by:

$$\boldsymbol{f}(\boldsymbol{x}, t) = \boldsymbol{v}(\boldsymbol{x}, t)^T \boldsymbol{\mu} + Z(\boldsymbol{x}, t), \tag{3}$$

where $f(\boldsymbol{x}, t)$ is the response at input $\boldsymbol{x}$ and time point t, $\boldsymbol{v}(\boldsymbol{x}, t)^T = (1, v_1(\boldsymbol{x}, t), v_2(\boldsymbol{x}, t), \dots v_L(\boldsymbol{x}, t))$ is a set of known basis functions, and $\boldsymbol{\mu}$ is the corresponding parameter vector with length $(1 + L)$. It is assumed that $Z(\boldsymbol{x}, t)$ follows a Gaussian process with zero mean and covariance function $\sigma^2 \boldsymbol{r}(\boldsymbol{x}, t)$, where $\boldsymbol{r}(\boldsymbol{x}, t)$ is the correlation function which can be separated as below:

$$\boldsymbol{r}(\boldsymbol{x_1} - \boldsymbol{x_2}, t_1 - t_2) = \left(\prod_{i=1}^{p} r_i(x_{i1} - x_{i2})\right) r_T(t_1 - t_2), \tag{4}$$

where $r_i(x_{i1} - x_{i2}) = \exp\{-\alpha_i (x_{i1} - x_{i2})^2\}$ and $r_T(t_1 - t_2) = \exp\{-\beta (t_1 - t_2)^2\}$. Let $\xi = (\alpha_1, \dots, \alpha_p, \beta)$.

Suppose all the functional responses are rearranged into one $N \times 1$ vector $f = (f_1^T, \dots, f_n^T)$, where $N = n \times m$, n is the number of simulation runs, and m is the number of time points in each run. The input settings can be written in the form $\boldsymbol{X} = (\boldsymbol{1}_m^T \otimes \boldsymbol{x}_1, \dots, \boldsymbol{1}_m^T \otimes \boldsymbol{x_n})^T = (\boldsymbol{X}_1, \dots, \boldsymbol{X}_N)$ and the functional space can be represented as $\boldsymbol{T} = (\boldsymbol{t_1^T}, \dots, \boldsymbol{t_n^T})^T = (t_1, \dots, t_N)$.

Therefore, once I have the ξ in the correlation functions, I can easily predict the responses by:

$$\hat{f}(\boldsymbol{x}, t) = \boldsymbol{v}(\boldsymbol{x}, t)^T \hat{\boldsymbol{\mu}} + \boldsymbol{r}(\boldsymbol{x}, t) \boldsymbol{R}_{\boldsymbol{X},\boldsymbol{t}}^{-\boldsymbol{1}} (\boldsymbol{f} - \boldsymbol{V}\hat{\boldsymbol{\mu}}), , \tag{5}$$

where, $\boldsymbol{V} = (\boldsymbol{v}(\boldsymbol{X}_1, t_1), \dots, \boldsymbol{v}(\boldsymbol{X}_N, t_N))^T$, $\hat{\boldsymbol{\mu}} = (\boldsymbol{V}^T \boldsymbol{R}_{\boldsymbol{X},\boldsymbol{t}}^{-\mathbf{1}} \boldsymbol{V})^{-\mathbf{1}} \boldsymbol{V}^T \boldsymbol{R}_{\boldsymbol{X},\boldsymbol{t}}^{-\mathbf{1}} \boldsymbol{f}$, $\boldsymbol{r}(\boldsymbol{x}, t) = (r(\boldsymbol{x} - \boldsymbol{X}_1, t - t_1), \dots, r(\boldsymbol{x} - \boldsymbol{X}_N, t - t_N))^T$, and $\boldsymbol{R}_{\boldsymbol{X},\boldsymbol{t}}$ is the $N \times N$ correlation matrix.

In order to estimate the correlation parameters ξ, the method introduced in [132] is utilized which minimizes the negative log- likelihood:

$$\hat{\xi} = argmin\left[N log\hat{\sigma}^2 + log\left|\boldsymbol{R}_{\boldsymbol{X},\boldsymbol{t}}\right|\right], \tag{6}$$

where $\hat{\sigma}^2 = \frac{1}{N}(\boldsymbol{f} - \boldsymbol{V}\hat{\boldsymbol{\mu}})^T \boldsymbol{R}_{\boldsymbol{X},\boldsymbol{t}}^{-\mathbf{1}} (\boldsymbol{f} - \boldsymbol{V}\hat{\boldsymbol{\mu}})$.

To get the optimal ξ from equation (6), $\boldsymbol{R}_{\boldsymbol{X},\boldsymbol{t}}^{-\mathbf{1}}$ and $\left|\boldsymbol{R}_{\boldsymbol{X},\boldsymbol{t}}\right|$ must be calculated multiple times, which is extremely computationally cost or even unachievable. Thus, specific procedures are needed to overcome the computation difficulty caused by functional responses.

In [113], the initial ξ is estimated by fitting two Gaussian processes of marginal profiles in $\boldsymbol{x}$ and t, which is the first stage. By including the interactions between $\boldsymbol{x}$ and t into $Z(\boldsymbol{x}, t)$ term in the equation (3), it can be expressed as:

$$\boldsymbol{f}(\boldsymbol{x}, t) = \mu_0 + \boldsymbol{k}^T(t)\boldsymbol{u}_t + \boldsymbol{g}^T(\boldsymbol{x})\boldsymbol{v}_{\boldsymbol{x}} + Z(\boldsymbol{x}, t), \tag{7}$$

where $\boldsymbol{k}(t) = \left(k_1(t), \dots, k_a(t)\right)^T$ and $\boldsymbol{g}(\boldsymbol{x}) = \left(g_1(\boldsymbol{x}), \dots, g_b(\boldsymbol{x})\right)^T$ are mean functions.

Suppose $\bar{e}_{.j} = \frac{1}{n}\sum_{i=1}^{n}(f_{ij} - \bar{f}_{i.})$, $\bar{f}_{i.} = \frac{1}{m}\sum_{j=1}^{m}(f_{ij})$, where $i = 1, \dots, n, j = 1, \dots m$. Based on $\bar{e}_{.1}, \dots, \bar{e}_{.m}$, and $\bar{f}_{1.}, \dots \bar{f}_{n.}$, equation (10) and (11) are individually fitted:

$$\bar{e}(t) = \mu_{t0} + \boldsymbol{k}^T(t)\boldsymbol{u}_t + Z(t), \tag{8}$$

$$\bar{f}(\boldsymbol{x}) = \mu_{x0} + \boldsymbol{g}^T(\boldsymbol{x})\boldsymbol{v}_{\boldsymbol{x}} + Z(\boldsymbol{x}), \tag{9}$$

where $Z(t) \sim GP(0, {\sigma_e}^2 r_T(\cdot))$ and $Z(\boldsymbol{x}) \sim GP(0, {\sigma_y}^2 r_{\boldsymbol{x}}(\cdot))$

The correlation parameters estimated in this stage are indexed as $\xi^{(0)} = (\alpha_1^{(0)}, \dots \alpha_p^{(0)}, \beta^{(0)})$, which will be used in the following stage.

In the case where functional responses are collected over a regular grid, it is easy to calculate $\boldsymbol{R_{X,t}} = \boldsymbol{R_X} \otimes \boldsymbol{R_t}$ based on the product correlation assumption [111]. $\boldsymbol{R_X}$ and $\boldsymbol{R_t}$ are individually the correlation matrix of $\boldsymbol{x}$ and t. Similarly, it is reasonable to get $\boldsymbol{R_{X,t}^{-1}} = \boldsymbol{R_X^{-1}} \otimes \boldsymbol{R_t^{-1}}$**.** By the Kronecker product assumption, the computation complexity is reduced to a large extent, which makes the minimizing negative log-likelihood method work for kriging model with functional responses.

To prepare for the following calibration process, both computer model $\boldsymbol{f}(\boldsymbol{x}, t)$ and discrepancy model $\boldsymbol{\delta}(\boldsymbol{x_o}, t)$ should be represented as functional Gaussian process models. I denote that $\boldsymbol{x_o} = \left(x_{o1}, \dots, x_{op_1}\right)^T$ are the input variables and $\boldsymbol{\eta} = \left(\eta_1, \dots, \eta_{p_2}\right)^T$ are the calibration parameters. Note that $\boldsymbol{x} = \left(x_{o1}, \dots, x_{op_1}, \eta_1, \dots, \eta_{p_2}\right)^T = (\boldsymbol{x_o^T}, \boldsymbol{\eta_o^T})^T$. Thus, the discrepancy model can be represented as:

$$\delta(\boldsymbol{x_o}, t) = \boldsymbol{v_\delta}(\boldsymbol{x_o}, t)^T \boldsymbol{\mu_\delta} + Z_\delta(\boldsymbol{x_o}, t). \tag{10}$$

Suppose $Z_\delta(\boldsymbol{x_o}, t) \sim GP\left(0, \tau^2 \boldsymbol{r_\delta}(\boldsymbol{x_o}, t)\right)$, where $\boldsymbol{r_\delta}(\boldsymbol{x_o}, t)$ is a Gaussian correlation function of model bias, which can be separated as below:

$$\boldsymbol{r_\delta}(\boldsymbol{x_{o1}} - \boldsymbol{x_{o2}}, t_1 - t_2) = \left(\prod_{i=1}^{p_1} r_{\delta i}(x_{oi1} - x_{oi2})\right) r_{\delta T}(t_1 - t_2), \tag{11}$$

where $r_{\delta i}(x_{oi1} - x_{oi2}) = \exp\{-\alpha_{\delta i}(x_{oi1} - x_{oi2})^2\}$ and $r_{\delta T}(t_1 - t_2) = \exp\{-\beta_\delta (t_1 - t_2)^2\}$. Let $\xi_\delta = (\alpha_{\delta 1}, \dots, \alpha_{\delta p_1}, \beta_\delta)$ are the correlation parameters for model discrepancy.

Similar to the computer model, suppose the discrepancy responses are rearranged into one $N_\delta \times 1$ vector $\delta = (\delta_1^T, \dots, \delta_{n_\delta}^T)$, where $N_\delta = n_\delta \times m$, n_δ is the number of experiment runs, and m is the same as above. The input settings can be written in the form $\boldsymbol{X_o} = (\boldsymbol{1}_m^T \otimes \boldsymbol{x}_{o1}, \dots, \boldsymbol{1}_m^T \otimes \boldsymbol{x_{on_\delta}})^T = (\boldsymbol{X}_{o1}, \dots, \boldsymbol{X}_{oN_\delta})$ and the functional space can be represented as $\boldsymbol{T_o} = (\boldsymbol{t}_1^T, \dots, \boldsymbol{t}_{n_\delta}^T)^T = (t_1, \dots, t_{N_\delta})$. Then the responses can be predicted by:

$$\hat{\delta}(\boldsymbol{x_o}, t) = \boldsymbol{v_\delta}(\boldsymbol{x_o}, t)^T \hat{\boldsymbol{\mu}}_\delta + \boldsymbol{r_\delta}(\boldsymbol{x_o}, t) \boldsymbol{R_{X_o,t}^{-1}} (\boldsymbol{\delta} - \boldsymbol{V_\delta} \hat{\boldsymbol{\mu}}_\delta), \tag{12}$$

where $\boldsymbol{V_\delta} = (\boldsymbol{v_\delta}(\boldsymbol{X}_{o1}, t_1), \dots, \boldsymbol{v_\delta}(\boldsymbol{X}_{oN_\delta}, t_{N_\delta}))^T$, $\widehat{\boldsymbol{\mu}}_{\boldsymbol{\delta}} = (\boldsymbol{V_\delta^T R_{X_o,t}^{-1} V_\delta})^{-1} \boldsymbol{V_\delta^T R_{X_o,t}^{-1} \delta}$, $\boldsymbol{r_\delta}(\boldsymbol{x_o}, t) = \left(r_\delta(\boldsymbol{x_o} - \boldsymbol{X}_{o1}, t - t_1), \dots, r(\boldsymbol{x_o} - \boldsymbol{X}_{oN_\delta}, t - t_{N_\delta})\right)^T$, and $\boldsymbol{R_{X_o,t}}$ is the $N_\delta \times N_\delta$ correlation matrix.

The correlation parameter set $\hat{\xi}_\delta$ can be estimated by:

$$\hat{\xi}_\delta = argmin\left[N_\delta log\hat{\tau}^2 + log\left|\boldsymbol{R_{\delta X_o,t}}\right|\right], \tag{13}$$

where $\hat{\tau}^2 = \frac{1}{N_\delta}(\boldsymbol{\delta} - \boldsymbol{V_\delta}\widehat{\boldsymbol{\mu}}_{\boldsymbol{\delta}})^T \boldsymbol{R_{X_o,t}^{-1}}(\boldsymbol{\delta} - \boldsymbol{V_\delta}\widehat{\boldsymbol{\mu}}_{\boldsymbol{\delta}})$.

There are in total six input variables and two calibration parameters as listed in Table 3. Three of them are related to printing process: layer thickness (x_1), printing speed (x_2), nozzle temperature (x_3); and four are related to the layer (x_4), printing pattern direction (x_5), and neighborhood time difference (NTD) (x_6). The concept of NTD is used to index the specific time location along the printing path on a printed layer, which is explained in details in the Appendix A [133]. The two calibration parameters are natural heat convection coefficient for air (η_1) and latent heat of fusion (η_2), which are treated as fixed values during the whole printing process. I use 16 sets of model input variables for data training in surrogate modeling, with the values of each set of input variables determined by the nested space filling design method [134], as shown in Table 4.

Table 3. Input variables and calibration parameters list.

Input Variables		Calibration Parameters
Printing Settings	Index Variables	
• Layer thickness • Printing speed • Nozzle temperature	• Layer index • Printing pattern direction • NTD	• Natural convection coefficient • Latent heat of fusion

Table 4. Surrogate modeling: design of experiments (DOE) for computer simulations.

Runs	x_1 $[mm]$	x_2 $[mm/s]$	x_3 $[K]$	η_1 $[W/(m^2K)]$	η_2 $[J/g]$
1	0.27	44	493.15	11	18

2	0.15	28	499.83	7	20
3	0.19	46	506.51	8	10
4	0.23	36	494.82	9	34
5	0.16	20	496.49	3	12
6	0.28	22	513.19	10	26
7	0.24	48	501.50	4	28
8	0.25	30	514.86	12	14
9	0.17	50	516.53	15	36
10	0.26	24	508.18	16	22
11	0.18	38	509.85	13	30
12	0.20	26	503.17	14	38
13	0.29	32	511.52	5	40
14	0.21	40	518.20	6	24
15	0.30	42	504.84	17	16
16	0.22	34	498.16	18	32

3.4.2 Experimental data collection from quasi in situ thermal imaging: spatial-temporal registration

Once the surrogate model is constructed for the 3D FEA model, the experimental data of thermal field can be collected for Bayesian calibration. I use a spatial-temporal registration method to map the temperature distribution along the printing path. For the experimental data, the pixels in each IR image are ordered by the printing sequence as demonstrated by Figure 21 in Appendix A. As a

result, a 2D IR image in the spatial space can be transformed to a 1D temporal space vector based on the engineering knowledge instead of simply concatenating the pixels line by line [135, 136]. One example is shown in Figure 10, which corresponds to the same sample and process setting as in Figures 7 and 8. Using the spatial-temporal registration method, the as-measured thermal image in Figure 9 (b) is transformed to a curve in Figure 10 based on the printing path information in Figure 8 (a) and (b). This curve shows that the temperature generally increases along the printing path owing to the energy input associated with the deposition of new materials during printing. However, the high temperature points at the first half of the printing process are against this trend. By mapping these points back to the 2D image and investigating the printing path in detail, I conclude that these high temperature points originate from the reheating effects, as they are close to the deposition region.

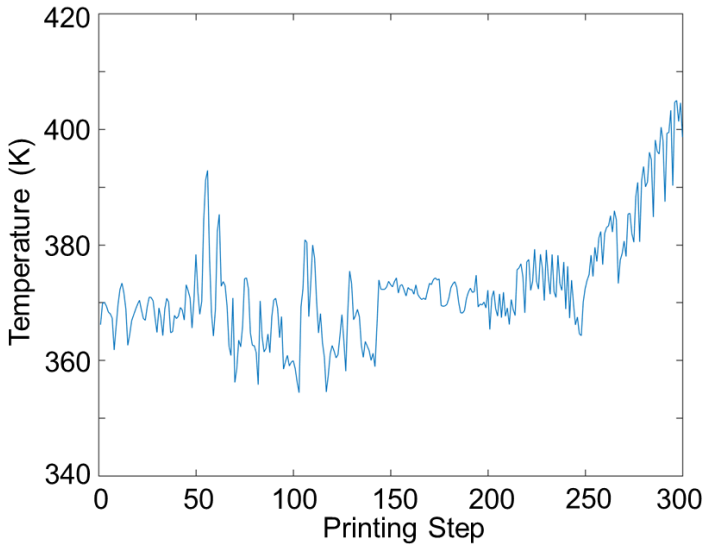

Figure 10. Temperature measurement of Layer 5 in g_1 component at $t = 334.5s$ represented along printing path (unit: K).

While the simulation results can be collected with the temporal resolution of $0.03\ s$, the IR images can only be collected discretely after a layer is finished, like snapshots (Figure 11). As a result, I only use the layer-to-layer thermal field as the model output. Because the length of the printing path is different for each layer, spline interpolation [137] is conducted to guarantee the same length for every sample so that the problem can be fitted into a regular grid and solved efficiently [113]. In addition, the simulation model has a spatial resolution of $0.5\ mm$ as determined by the G-code,

but the IR images have coarser resolution around 1 mm per pixel. To align these two data sets, the simulated temperature values are averaged over $1 \times 1\ mm^2$ areas.

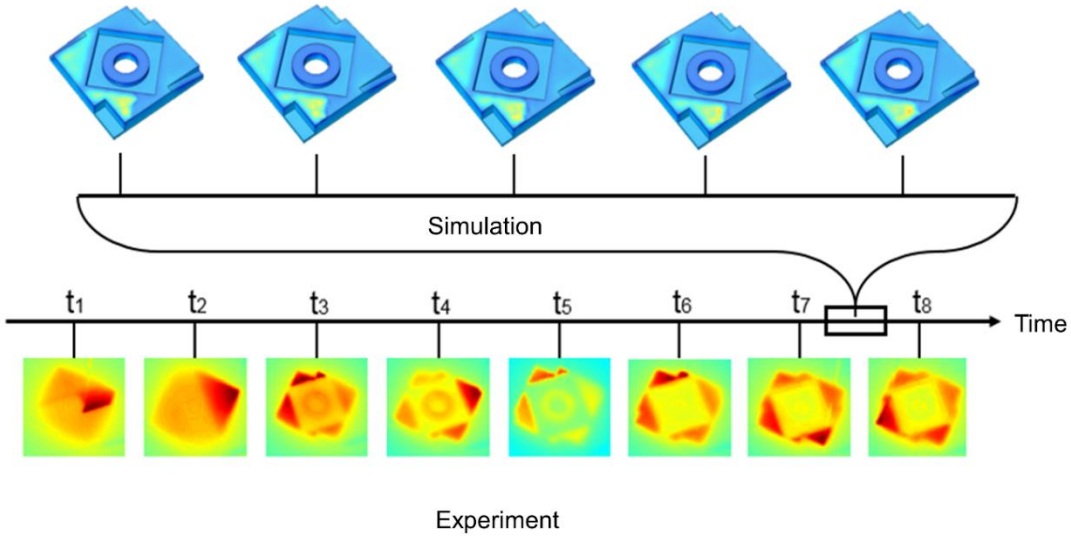

Figure 11. A comparison between the temporal resolution of simulation and experiment. The simulation has a temporal resolution of 0.03 s , while the experiment is layer-to-layer.

3.4.3 Online Updating Bayesian Calibration

After obtaining the experimental data and simulation data, I am able to conduct Bayesian calibration. The basic idea about Bayesian calibration introduced here is from Kennedy and O'Hagan [8]. Suppose $\boldsymbol{y}$ be the output of the actual experiment, $\boldsymbol{f}(\boldsymbol{x_o}, \boldsymbol{\eta}, t)$ the engineering model, $\boldsymbol{\delta}(\boldsymbol{x_o}, t)$ is model bias or discrepancy function, and $\epsilon \overset{iid}{\sim} N(0, \lambda^2)$ is the observation or measurement error. Then the model is expressed as:

$$\boldsymbol{y} = \boldsymbol{f}(\boldsymbol{x_o}, \boldsymbol{\eta}, t) + \boldsymbol{\delta}(\boldsymbol{x_o}, t) + \epsilon. \tag{16}$$

Combine simulation outputs with experiment ones, I get $\boldsymbol{d}^T = (\boldsymbol{y}^T, \boldsymbol{f}^T)$. Combine simulation and experiments design points as introduced in [8], I then get $\boldsymbol{x_{Total}}(\boldsymbol{\eta})$ by:

$$\boldsymbol{x_{Total}}(\boldsymbol{\eta}) = \begin{pmatrix} \boldsymbol{D_1} & \boldsymbol{0} \\ \boldsymbol{D_2(\eta)} & \boldsymbol{D_2} \end{pmatrix}, \tag{17}$$

where $\boldsymbol{D_1} = \boldsymbol{x}$ and $\boldsymbol{D_2} = \boldsymbol{x_o}$ individually denote the design points of computer model and experiment model, and $\boldsymbol{D_2}(\boldsymbol{\eta}) = \{(\boldsymbol{x_{o1}}, \boldsymbol{\eta}), \dots, (\boldsymbol{x_{on_\delta}}, \boldsymbol{\eta})\}$ are the integration of experiment model design points and calibration parameters.

The functional kriging model for the combined data set can be given by:

$$\boldsymbol{d}(\boldsymbol{x_{Total}}, t) = \boldsymbol{v_{Total}}(\boldsymbol{x_{Total}}, t)^T \boldsymbol{\mu_{Total}} + Z_{Total}(\boldsymbol{x_{Total}}, t), \tag{18}$$

where $\boldsymbol{v_{Total}}(\boldsymbol{x_{Total}}, t)^T = (1, v_{Total,1}(\boldsymbol{x_{Total}}, t), v_{Total,2}(\boldsymbol{x_{Total}}, t), \dots v_{Total,L_{Total}}(\boldsymbol{x_{Total}}, t))$ is a set of known functions, and $\boldsymbol{\mu_{Total}}$ is the corresponding parameter vector with length $(1 + L_{Total})$. It is assumed that $Z_{Total}(\boldsymbol{x_{Total}}, t)$ follows a Gaussian process with zero mean and covariance function $\sigma^2_{Total}\boldsymbol{r_{Total}}(\boldsymbol{x_{Total}}, t)$. Similar to equation (4, 11), the covariance function can be separated to input space and functional space as:

$$\boldsymbol{r_{Total}}(\boldsymbol{x_{Total,1}} - \boldsymbol{x_{Total,2}}, t_1 - t_2) = \left(\prod_{i=1}^{p+p1} r_{Total,i}(x_{Total,i1} - x_{Total,i2})\right) r_{Total,T}(t_1 - t_2), \tag{19}$$

where $r_{Total,i}(x_{Total,i1} - x_{Total,i2}) = \exp\left\{-\alpha_{Total,i}(x_{Total,i1} - x_{Total,i2})^2\right\}$ and $r_{Total,T}(t_1 - t_2) = \exp\{-\beta_{Total}(t_1 - t_2)^2\}$. Let $\xi_{Total} = (\alpha_1, \dots, \alpha_p, \alpha_{\delta 1}, \dots, \alpha_{\delta p_1}, \beta_{Total})$, which are all estimated in Section 3.4.1 except for β_{Total}. Thus, in the following stage, both β_{Total} and calibration parameters should be inferenced.

The combination outputs can be predicted by:

$$\hat{d}(\boldsymbol{x}, t) = \boldsymbol{v_{Total}}(\boldsymbol{x_{Total}}, t)^T \hat{\boldsymbol{\mu}}_{\boldsymbol{Total}} + \boldsymbol{r_{Total}}(\boldsymbol{x_{Total}}, t)\boldsymbol{R}^{-1}_{\boldsymbol{X_{Total},t}}(\boldsymbol{d} - \boldsymbol{V_{Total}}\hat{\boldsymbol{\mu}}_{\boldsymbol{Total}}), \tag{20}$$

where $\boldsymbol{V_{Total}}$, $\hat{\boldsymbol{\mu}}_{\boldsymbol{Total}}$, $\boldsymbol{r_{Total}}(\boldsymbol{x_{Total}}, t)$, and $\boldsymbol{R}^{-1}_{\boldsymbol{X_{Total},t}}$ are defined similarly to those in Section 3.4.1. Thus, the calibration parameters can be estimated by minimizing the negative log- likelihood:

$$\hat{\boldsymbol{\eta}} = argmin\left[N_{Total} log\hat{\sigma}^2_{Total} + log\left|\boldsymbol{R}_{\boldsymbol{X_{Total},t}}\right|\right], \tag{21}$$

where $N_{Total} = N + N_\delta$, $\hat{\sigma}^2_{Total} = \frac{1}{N_{Total}}(\boldsymbol{d} - \boldsymbol{V_{Total}}\hat{\boldsymbol{\mu}}_{\boldsymbol{Total}})^T \boldsymbol{R}^{-1}_{\boldsymbol{X_{Total},t}}(\boldsymbol{d} - \boldsymbol{V_{Total}}\hat{\boldsymbol{\mu}}_{\boldsymbol{Total}})$.

The posterior distribution of the calibration parameters can be calculated by:

$$p(\boldsymbol{\eta}|\boldsymbol{d},\hat{\boldsymbol{\xi}}) \propto p(\boldsymbol{d}|\boldsymbol{\eta},\hat{\boldsymbol{\xi}})p(\boldsymbol{\eta}), \tag{22}$$

$p(\boldsymbol{\eta})$ is the prior distribution of the calibration parameters. The likelihood function $p(\boldsymbol{d}|\boldsymbol{\eta},\hat{\boldsymbol{\xi}})$ is represented as in Equation (21). One of Markov Chain Monte Carlo (MCMC) methods, Metropolis–Hastings algorithm, is used here for obtaining a sequence of random samples from the posterior density, particularly from multi-dimensional distributions.

The main steps of Metropolis–Hastings algorithm is summarized as below:

- Beginning at a random initial parameter value.
- Selecting a new set of parameters close to the initial ones based on the proposal function
- Jumping to the new point with a probability $p(\boldsymbol{\eta}_{new}|\boldsymbol{d},\hat{\boldsymbol{\xi}})/p(\boldsymbol{\eta}_{new}|\boldsymbol{d},\hat{\boldsymbol{\xi}})$.

By the above steps, MCMC can sample from the posterior and calculate the desired posterior quantities of the calibration parameters.

Since the temperature information is registered along the printing path, the error term has a time series structure, which violates the independent and identically distributed (iid) assumption made in [8]. I therefore propose an online updating Bayesian calibration method to consider the autocorrelation of the error term. "Online updating" here means that the observation error term is of a time series structure, and its prediction at a given time t is influenced by the values at previous times. This is in contrast with conventional Bayesian calibration like in [8], where the observation error is a white noise and unrelated to real-time measurements.

The autoregressive (AR) model [138] is used to identify the pattern from the error term, which can be rewritten as:

$$\varepsilon_t = \alpha + \phi_1\varepsilon_{t-1} + \phi_2\varepsilon_{t-2} + \cdots + \phi_k\varepsilon_{t-k} + \omega_t. \tag{23}$$

Here $\omega_t \overset{iid}{\sim} N(0,\sigma^2)$ is the white noise term, α is the intercept, and $\boldsymbol{\Phi} = [\phi_1, \ldots, \phi_k]^T$ are the coefficients to indicate the relationship between the current error with the previous k ones. The possible autocorrelation in the observation error is removed with the first-order AR model ($AR(1)$) in the error term (see Appendix B for details). After obtaining the coefficient and intercept of the

$AR(1)$ model from the training samples, the response of a new testing sample can be estimated accordingly.

I conduct the Bayesian calibration by comparing the experimental data and surrogate modeling results and estimating the values of hyperparameters and calibration parameters. In general, the number of available experimental samples is limited, as it takes more resources (e.g. materials and equipment) to run the actual manufacturing processes and temperature measurements. Thus, properly selecting representative sets of experimental conditions using DOE methods is essential. As shown in Table 5, using the maxi-min distance criteria [139], four different input settings with two replicates of each are selected for Bayesian calibration. With the calibrated model, the proposed framework will allow for thermal field prediction of components with different process settings and geometric designs, as shown in the following.

Table 5. Bayesian calibration: DOE for physical experiments.

Runs	x_1 $[mm]$	x_2 $[mm/s]$	x_3 $[K]$
1	0.27	44	493.15
2	0.16	20	496.49
3	0.28	22	513.19
4	0.17	50	516.53
5	0.28	22	513.19
6	0.27	44	493.15
7	0.16	20	496.49
8	0.17	50	516.53

Chapter 4: Results and Discussion

4.1 Data training plans

To evaluate the performance of the proposed framework, I use it for two types of thermal field prediction, i.e. prediction with different process settings and prediction with different component geometric designs. These correspond to two data training plans: (i) "leave one setting out" (Training Plan 1), which uses the experimental data of six samples to predict the remaining two samples with the same geometry but different process settings; (ii) "leave one geometry out" (Training Plan 2), which uses the experimental data of the two geometries to predict the remaining geometry. These two training plans are illustrated in Figures 12 and 13.

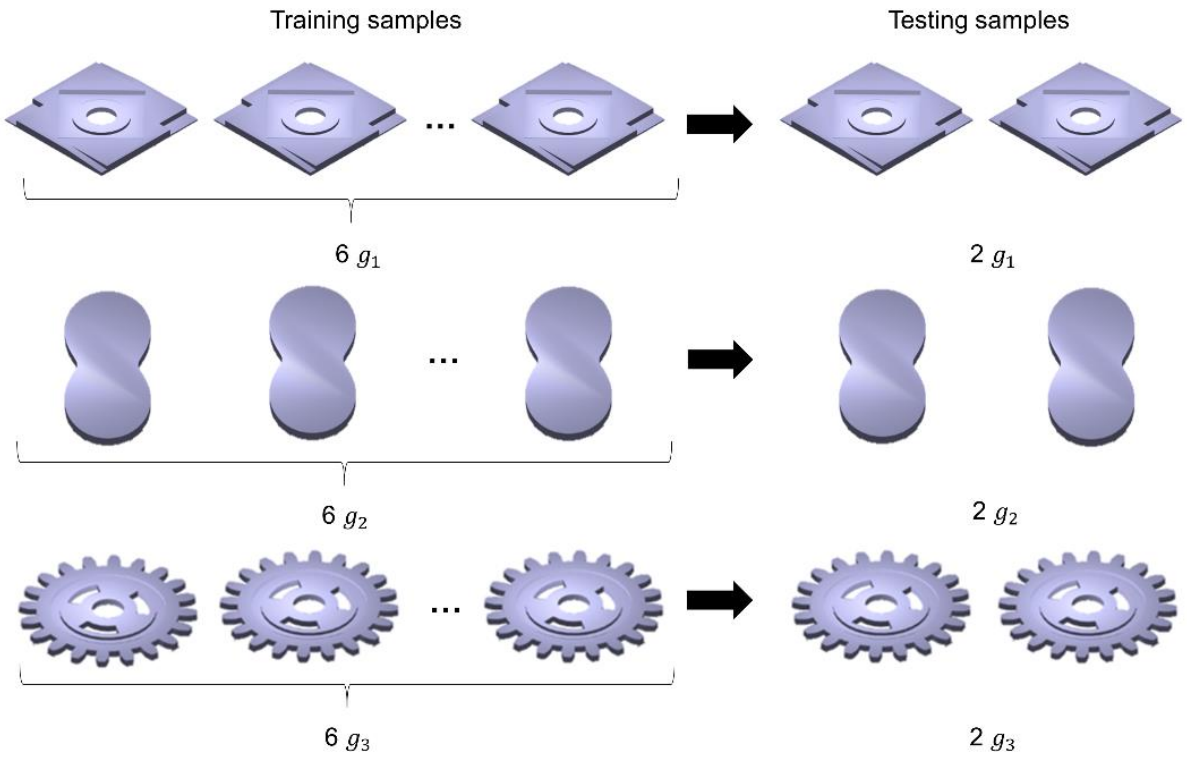

Figure 12. Training Plan 1: "leave one setting out".

In Training Plan 1, every time two samples with the same process setting are left out as the testing data, with the six remaining samples being used as the training data. In the end, I get eight prediction evaluations, with the mean value representing the final prediction performance. The

experimental samples are selected to best cover the future potential process settings, so Training Plan 1 is used to test if the proposed framework works well in the whole feasible design space of $x_1 \sim x_3$. In Training Plan 2, I aim to predict for a new component geometry by using the experimental data of two different geometries.

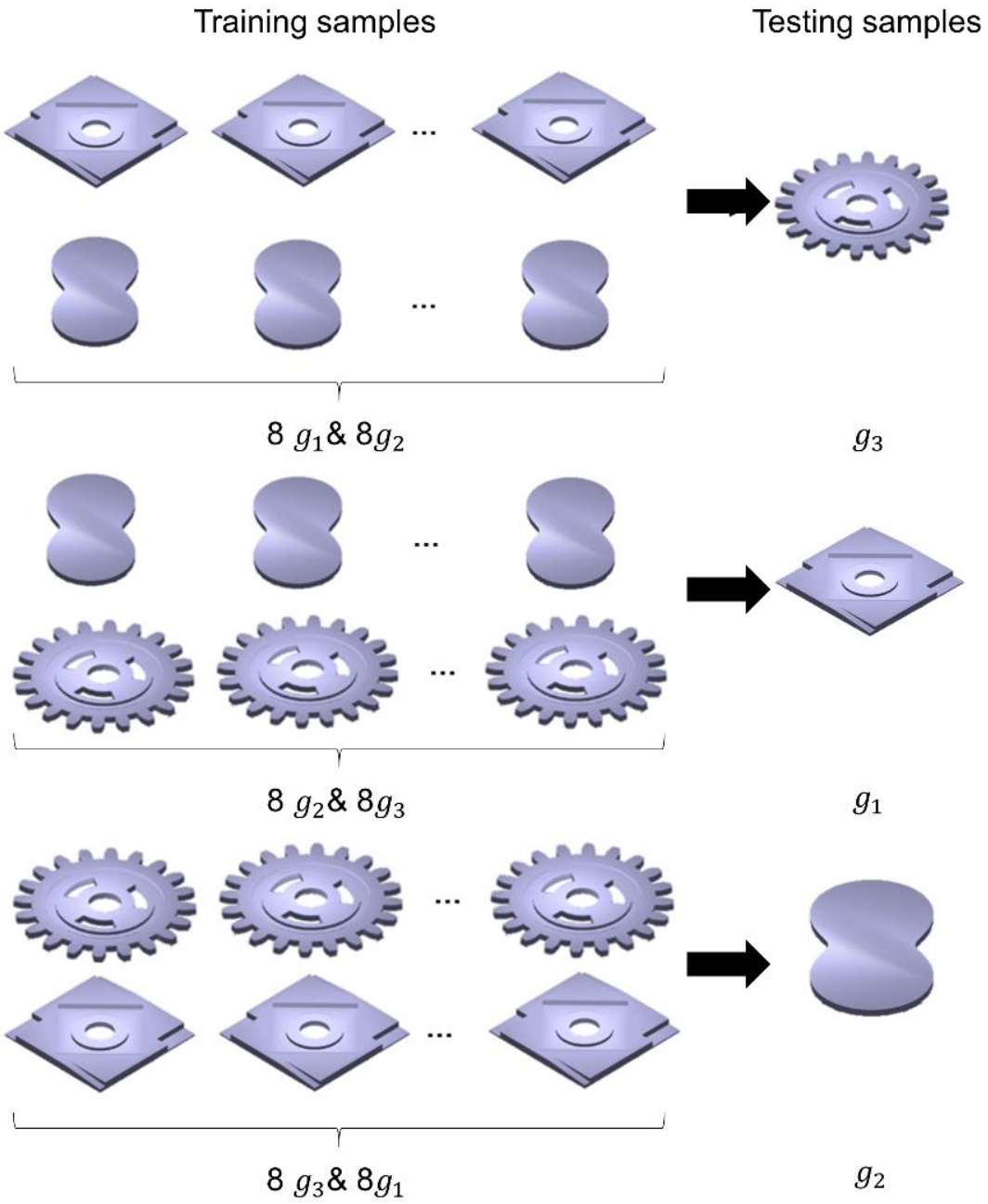

Figure 13. Training Plan 2: “leave one geometry out”.

4.2 Prediction for different process settings using Training Plan 1

Training Plan 1 is applied for prediction with different process settings, including layer thickness, printing speed, and nozzle temperature. I use the root mean square error (RMSE) to represent the difference between the predicted values and actual experiments. Through cross-validation, the proposed framework leads to a RMSE of 5.55 K for g_1, 5.87 K for g_2, and 5.70 K for g_3, respectively, which is independent on component geometry. The averaged RMSE for these three geometries is 5.71 K, which is 1.23% of the maximum measured temperature. Figure 14 shows the comparison between the results from the proposed calibrated model and the original simulation. The computational time for building the physically-based simulation models is 17.42 h, 6.84 h, and 15.12 h for g_1, g_2, and g_3, respectively, with an averaged value of 13.13 h. For comparison, the averaged computational time for predicting one component using the proposed framework is 0.31 h, which is more than 40 times faster compared to the FEA simulation models.

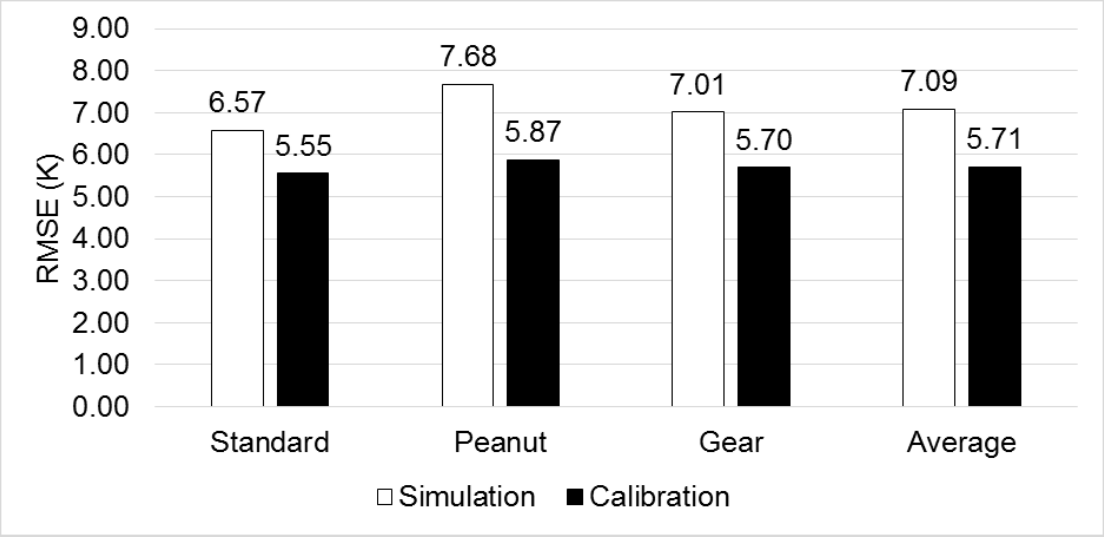

Figure 14. RMSEs comparison between the simulation and the proposed calibration model for training plan 1.

To validate the model error *iid* assumption, residual plots are drawn separately for two cases: the ordinary calibration approach without considering autocorrelation and the proposed calibration approach considering autocorrelation. Figure 15 shows the 2D distribution of residuals and the $\hat{\varepsilon}_t$

$vs\ \hat{\varepsilon}_{t-1}$plot. The residuals are randomly distributed in the latter case (Figure 15 (c)) but not in the former case (Figure 15 (a)). The $\hat{\varepsilon}_t\ vs\ \hat{\varepsilon}_{t-1}$ plot of the proposed model (Figure 15 (d)) does not have apparent patterns like Figure 15 (b), where a linear increasing trend can be found. By considering the autocorrelation in the error term, therefore, the proposed model better captures the autoregressive pattern in the discrepancy term, and further improves the prediction performance.

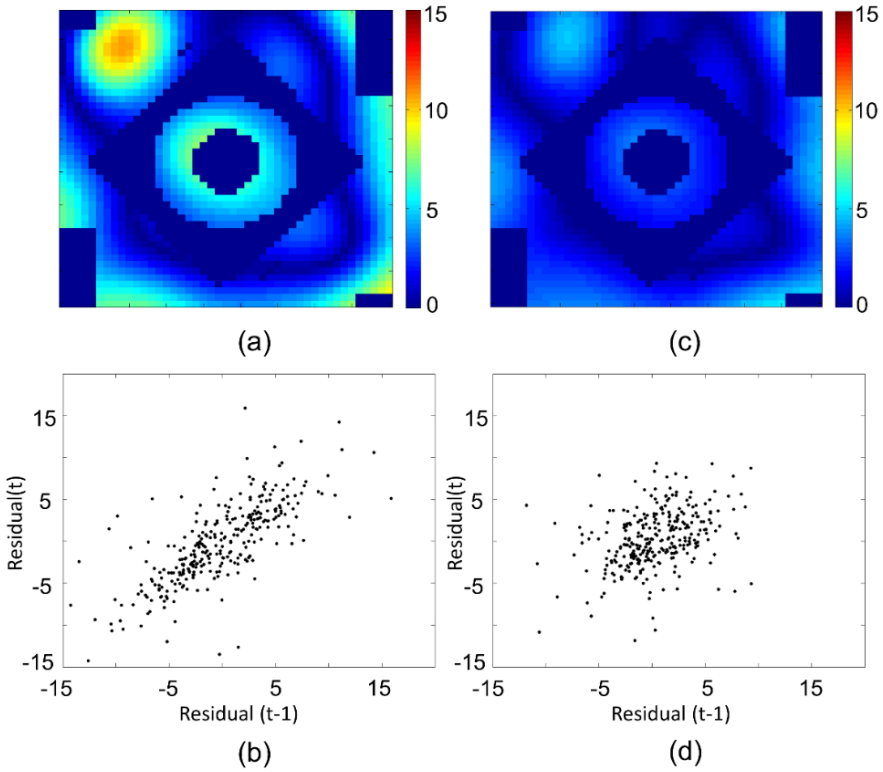

Figure 15. Diagnosis plots using the ordinary calibration approach without considering autocorrelation: (a) $|\hat{\varepsilon}|$ in 2D; (b) $\hat{\varepsilon}_t\ vs\ \hat{\varepsilon}_{t-1}$; and using the proposed calibration approach considering autocorrelation: (c) $|\hat{\varepsilon}|$ in 2D; (d) $\hat{\varepsilon}_t\ vs\ \hat{\varepsilon}_{t-1}$ (unit: K).

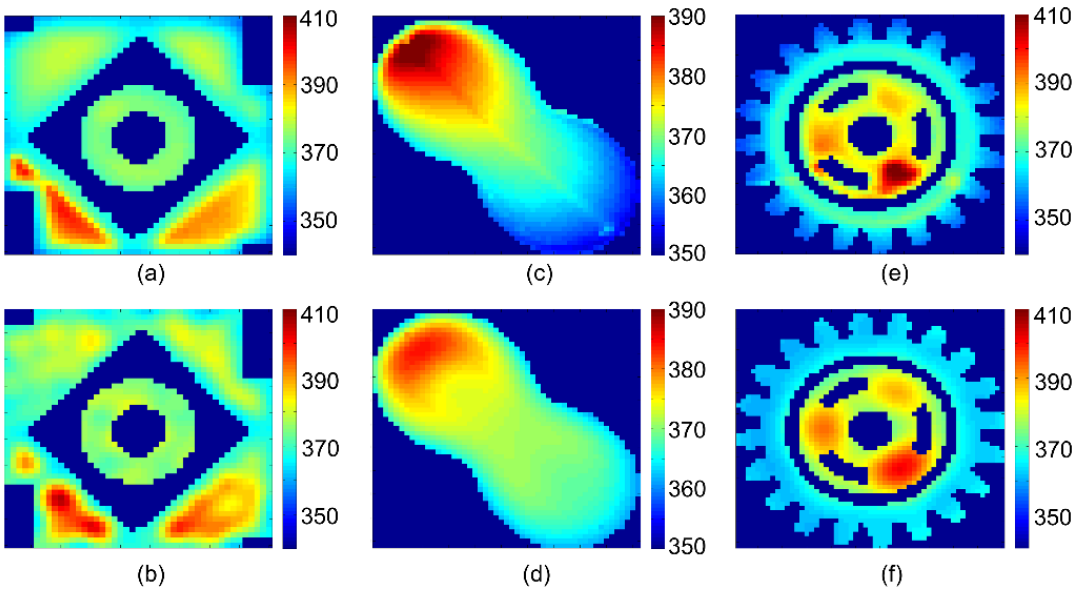

Figure 16. (a), (c), (e): temperature measurements for a layer in g_1, g_2, and g_3. (b), (d), (f): predictions using Training Plan 1 (unit: K).

Figure 16 shows a representative comparison of the thermal field from the actual experiments (the first row) and prediction results (the second row). Here, (a) and (b) are the thermal field of Layer 6 of a g_1 component at the process setting specified in Line 6 in Table 5; (c) and (d) are the thermal field of Layer 7 of a g_2 component at the process setting specified in Line 2 in Table 5; (e) and (f) are the thermal field of Layer 6 of a g_3 component at the process setting specified in Line 6 in Table 5. With only six data sets used for training, the prediction results well match the experiments with the RMSE of 5.51 K, 4.86 K, and 5.56 K in these specific examples.

Uncertainty quantification is evaluated using the same layer and same process setting as those in Figure 16. The 95% confidence interval for the prediction (illustrated in Figure 17) is given by [132], which is decided by the upper 0.25 critical point of the standard normal distribution, correlation matrix, and known basis functions. The blue solid line represents the actual experimental measurement, and the black dashed line shows the predicted temperature by the proposed framework. The red dashed lines illustrate the upper and lower bounds of the 95% confidence interval, where the averaged confidence interval width for the three samples are 21.61 K, 20.51 K, and 14.23 K, respectively. Almost all of the observations (blue line) are in the

acceptable range (grey area). The results in Figs. 10 and 11 show that the proposed framework enables accurate thermal field prediction for different process settings in FDM.

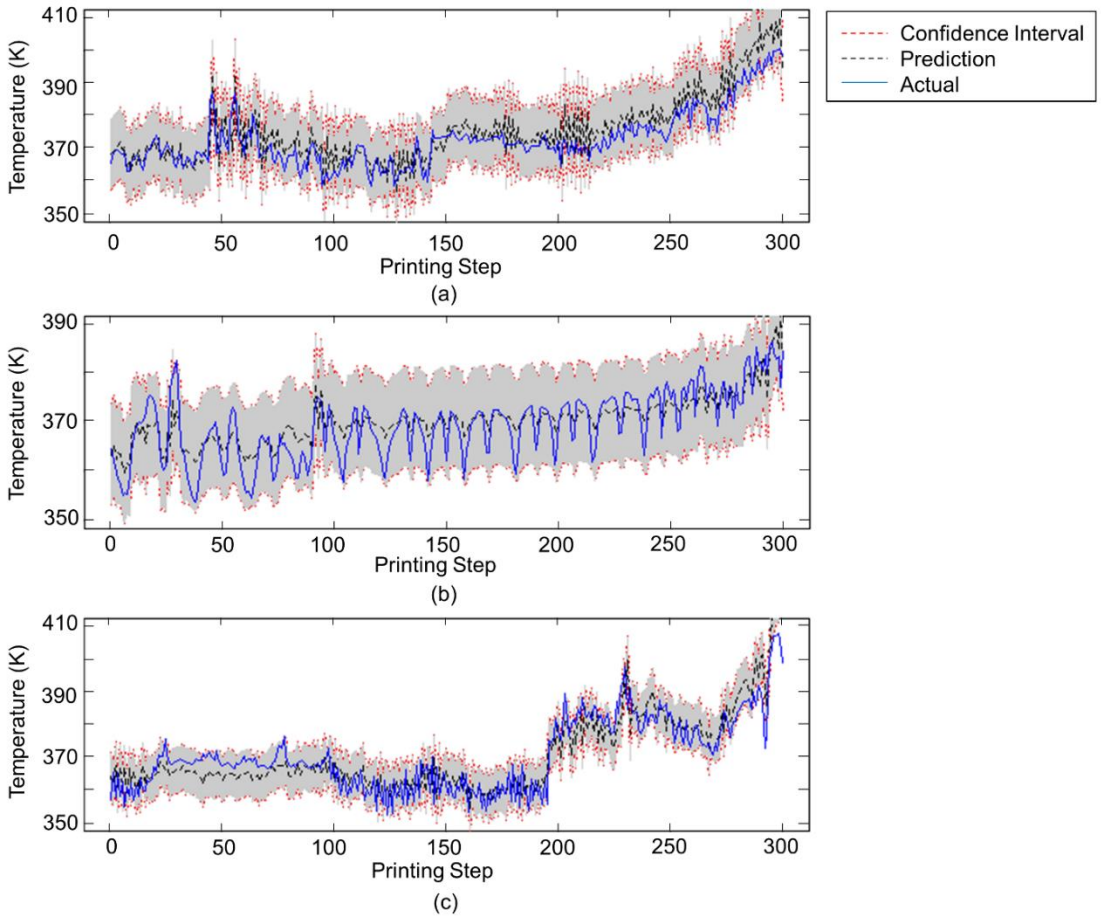

Figure 17. Prediction and 95% confidence interval in Training Plan 1 of (a) g_1, (b) g_2, and (c) g_3.

4.3 Prediction for different component geometries using Training Plan 2

From Training Plan 1, the mean and standard deviation values of the calibration parameters are determined and shown in Table 6. The averaged calibration values $\hat{\boldsymbol{\eta}} = (0.43, 0.30)$ in [0,1] correspond to the convection coefficient h ~9.45 $W/(m^2K)$ and latent heat of fusion L ~19.00 J/g. These values are consistent with other findings of PLA [129, 140]. It is interesting to note that the calibration results are similar for the three different geometries, suggesting a weak

dependence of calibration results on geometric designs. Figure 18 shows the discrepancy terms of the three geometries, which are generally within the same range and follow a similar decreasing trend at the end of printing.

Table 6. Estimated calibration parameters in [0, 1] interval of different geometry types.

Geometry Types	η_1 Mean	η_1 Standard Deviation	η_2 Mean	η_2 Standard Deviation
g_1	0.38	0.16	0.26	0.21
g_2	0.45	0.11	0.32	0.07
g_3	0.45	0.10	0.30	0.14
Average	0.43	0.12	0.30	0.14

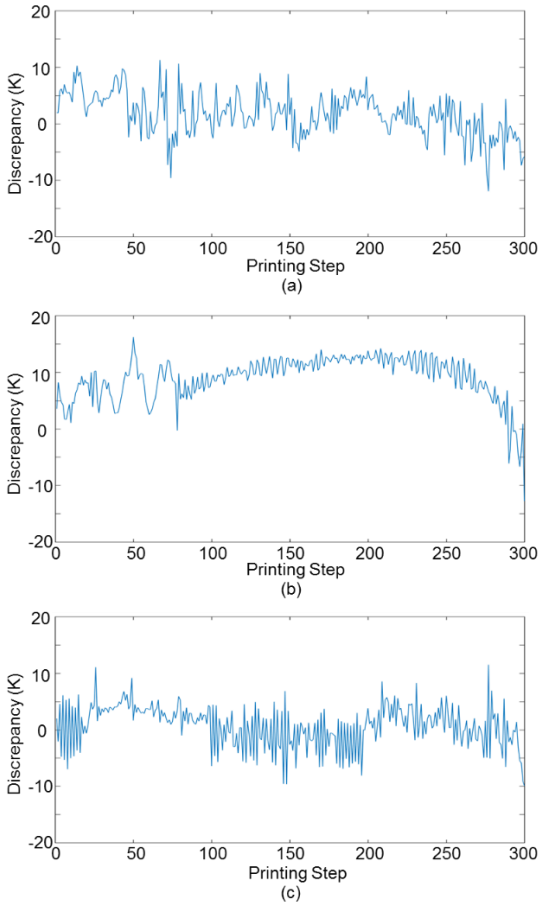

Figure 18. The discrepancy term (a) of g_1; (b) of g_2; (c) of g_3.

The proposed framework includes some geometry information as model inputs (e.g. printing pattern direction) and uses spatial-temporal registration to characterize the thermal field. With the weak geometric dependences of the calibration parameters and model discrepancy, I therefore hypothesize that the proposed data training and calibration approaches apply for different component geometries. To test this hypothesis, I evaluate the performances of the proposed framework using Training Plan 2. The cross-validation gives the RMSE results of 6.32 K for g_1, 5.12 K for g_2, and 6.97 K for g_3, respectively. The averaged RMSE for these three geometries is 6.14 K, which is 1.33% of the maximum measured temperature. As illustrated in Figure 19, the proposed model also has better prediction performances than the computer simulations in Training Plan 2. Figure 20 compares the layer-wise thermal field between the actual experimental measurements (the first row) and the prediction results of the "leave one geometry out" plan (the second row). Among the three geometric designs, the proposed framework has the best prediction performance in g_2 , which is of a relative simple smooth contour. In contrast, the contours of g_1 and g_3 are of complex geometric features. These features can lead to intricate printing path, which may cause unexpected reheating in the corresponding regions. This finding suggests that the proposed framework works best when using complicated geometries (like g_1 and g_3) to predict a simple geometry (like g_2).

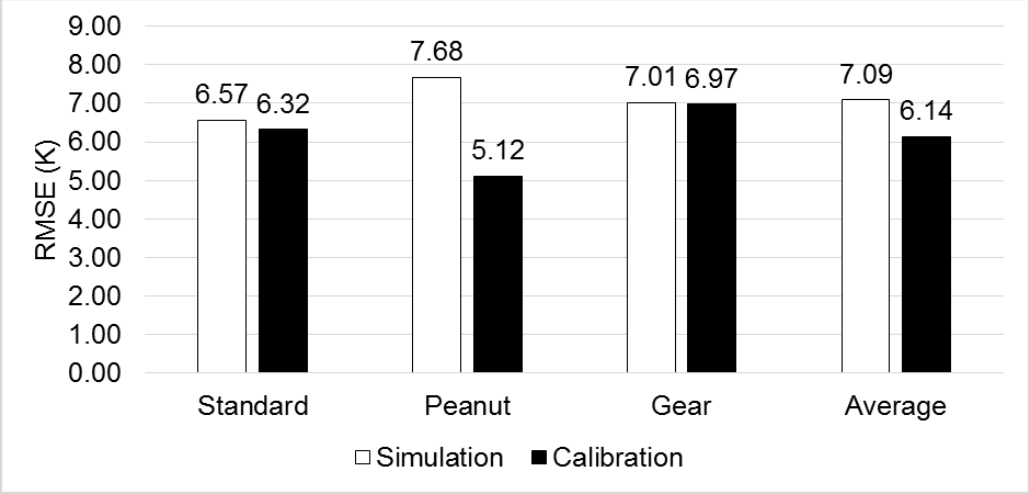

Figure 19. RMSEs comparison between the simulation and the calibration model considering autocorrelation for training plan 2.

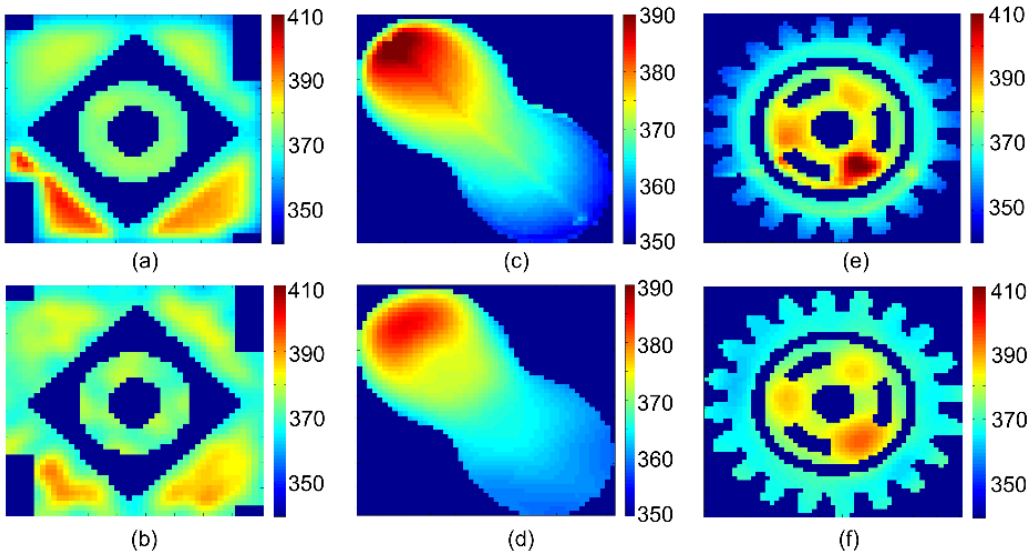

Figure 20. (a), (c), (e) Temperature measurements for g_1, g_2, and g_3; (b), (d), (f) temperature predictions for g_1, g_2, and g_3 in Training Plan 2 (unit: K).

In summary, the averaged testing RMSEs are $5.71\ K$ in Training Plan 1 and $6.14\ K$ in Training Plan 2, corresponding to 1.23% and 1.33% of the maximum measured temperature, respectively. These relatively small numbers show the success of using the proposed framework for component-scale prediction in AM processes. To compare with the previous work in literature, a selective laser sintering (SLS) process is investigated in reference [15] based on continuous media theory, where the maximum temperature value is compared between simulations and experiments with a relative prediction error percentage more than 5.00%. In reference [141], the maximum temperature during laser melting of metal powder is evaluated and the relative error of the FEA results from the experimental results [142] is 2.8%. It should be noted that the work in these references does not enable component-scale prediction, let alone the higher prediction error and higher computational cost as compared to the proposed framework.

Chapter 5: Summary and Conclusion

By integrating physically-based and data-driven approaches, I have developed a new framework to enable component-scale, layer-to-layer thermal field prediction in AM. The most significant contributions of this work are summarized as follows:

- A physically-based model using "element activation and deactivation" and adaptive mesh methods is constructed to investigate the layer-to-layer thermal field during AM processes. The CAD design file, G-code file, and process variables can be directly imported into the 3D FEA model, which makes it generally applicable to any geometry of freeform and under any process setting.
- To minimize the computational costs from the high-fidelity 3D FEA model, a data-driven surrogate model is built based on functional Gaussian process. By training the historical FEA results, the surrogate model effectively represents the relationship between process settings and model responses. A spatial-temporal registration method is proposed to map the layer-to-layer thermal field along the printing path, which enables the proposed framework for different geometric designs.
- Through Bayesian calibration, the final model not only determines the unknown parameters in the computer simulations but also explains and corrects for the model discrepancy. In particular, an online updating approach is proposed to remove the possible autocorrelation in the observation error.
- As shown by cross-validation, the proposed framework enables accurate and fast prediction of the layer-to-layer thermal field for components with different process settings and geometric designs. For the latter, the proposed framework shows better performance for predicting simple geometries using the complicated geometries as training data.

References

[1] N. Raghavan, R. Dehoff, S. Pannala, S. Simunovic, M. Kirka, J. Turner, N. Carlson, S.S. Babu, Numerical modeling of heat-transfer and the influence of process parameters on tailoring the grain morphology of IN718 in electron beam additive manufacturing, Acta Materialia 112 (2016) 303-314.

[2] S.W. Pattinson, A.J. Hart, Additive Manufacturing of Cellulosic Materials with Robust Mechanics and Antimicrobial Functionality, Advanced Materials Technologies (2017).

[3] G. D'Angelo, H.N. Hansen, A.J. Hart, Molecular Gastronomy Meets 3D Printing: Layered Construction via Reverse Spherification, 3D Printing and Additive Manufacturing 3(3) (2016) 152-159.

[4] J.J. Lewandowski, M. Seifi, Metal additive manufacturing: a review of mechanical properties, Annual Review of Materials Research 46 (2016) 151-186.

[5] J. Go, A.J. Hart, A framework for teaching the fundamentals of additive manufacturing and enabling rapid innovation, Additive Manufacturing 10 (2016) 76-87.

[6] A.G. Stevens, C.R. Oliver, M. Kirchmeyer, J. Wu, L. Chin, E.S. Polsen, C. Archer, C. Boyle, J. Garber, A.J. Hart, Conformal Robotic Stereolithography, 3D Printing and Additive Manufacturing 3(4) (2016) 226-235.

[7] D. Riedlbauer, M. Drexler, D. Drummer, P. Steinmann, J. Mergheim, Modelling, simulation and experimental validation of heat transfer in selective laser melting of the polymeric material PA12, Computational Materials Science 93 (2014) 239-248.

[8] M.C. Kennedy, A. O'Hagan, Bayesian calibration of computer models, Journal of the Royal Statistical Society: Series B (Statistical Methodology) 63(3) (2001) 425-464.

[9] H. Bikas, P. Stavropoulos, G. Chryssolouris, Additive manufacturing methods and modelling approaches: a critical review, The International Journal of Advanced Manufacturing Technology 83(1-4) (2016) 389-405.

[10] T. Craeghs, S. Clijsters, J.-P. Kruth, F. Bechmann, M.-C. Ebert, Detection of process failures in layerwise laser melting with optical process monitoring, Physics Procedia 39 (2012) 753-759.

[11] M.R. Bouschlicher, M.A. Vargas, D.B. Boyer, Effect of composite type, light intensity, configuration factor and laser polymerization on polymerization contraction forces, American journal of dentistry 10(2) (1997) 88-96.

[12] A. Bellini, S. Güçeri, Mechanical characterization of parts fabricated using fused deposition modeling, Rapid Prototyping Journal 9(4) (2003) 252-264.

[13] J. Cesarano, A review of robocasting technology, MRS Online Proceedings Library Archive 542 (1998).

[14] H. Sirringhaus, T. Kawase, R. Friend, T. Shimoda, M. Inbasekaran, W. Wu, E. Woo, High-resolution inkjet printing of all-polymer transistor circuits, Science 290(5499) (2000) 2123-2126.

[15] R. Sochol, E. Sweet, C. Glick, S. Venkatesh, A. Avetisyan, K. Ekman, A. Raulinaitis, A. Tsai, A. Wienkers, K. Korner, 3D printed microfluidic circuitry via multijet-based additive manufacturing, Lab on a Chip 16(4) (2016) 668-678.

[16] J.-P. Kruth, Material incress manufacturing by rapid prototyping techniques, CIRP Annals-Manufacturing Technology 40(2) (1991) 603-614.

[17] G. Chryssolouris, Manufacturing systems: theory and practice, Springer Science & Business Media2013.

[18] N.B. Dahotre, S. Harimkar, Laser fabrication and machining of materials, Springer Science & Business Media2008.

[19] L.E. Murr, S.M. Gaytan, D.A. Ramirez, E. Martinez, J. Hernandez, K.N. Amato, P.W. Shindo, F.R. Medina, R.B. Wicker, Metal fabrication by additive manufacturing using laser and electron beam melting technologies, Journal of Materials Science & Technology 28(1) (2012) 1-14.

[20] W.J. Sames, F. List, S. Pannala, R.R. Dehoff, S.S. Babu, The metallurgy and processing science of metal additive manufacturing, International Materials Reviews 61(5) (2016) 315-360.

[21] V. Beal, P. Erasenthiran, N. Hopkinson, P. Dickens, C.H. Ahrens, Scanning strategies and spacing effect on laser fusion of H13 tool steel powder using high power Nd: YAG pulsed laser, International journal of production research 46(1) (2008) 217-232.

[22] A. Boschetto, L. Bottini, Accuracy prediction in fused deposition modeling, The international journal of advanced manufacturing technology 73(5-8) (2014) 913-928.

[23] I. Yadroitsev, P. Krakhmalev, I. Yadroitsava, S. Johansson, I. Smurov, Energy input effect on morphology and microstructure of selective laser melting single track from metallic powder, Journal of Materials Processing Technology 213(4) (2013) 606-613.

[24] N.T. Aboulkhair, N.M. Everitt, I. Ashcroft, C. Tuck, Reducing porosity in AlSi10Mg parts processed by selective laser melting, Additive Manufacturing 1 (2014) 77-86.

[25] N. Read, W. Wang, K. Essa, M.M. Attallah, Selective laser melting of AlSi10Mg alloy: Process optimisation and mechanical properties development, Materials & Design (1980-2015) 65 (2015) 417-424.

[26] L. Wang, R. Jin, D. Henkel, K. Bourne, J. Burdick, Data Fusion for in situ Layer-wise Modeling and Feedforward Control of Selective Laser Melting Process, Submitted (2017).

[27] W. Sames, F. Medina, W. Peter, S. Babu, R. Dehoff, Effect of process control and powder quality on Inconel 718 produced using electron beam melting, Proceedings of the 8th International Symposium on Superalloy 718 and Derivatives, John Wiley & Sons, 2014, p. 409.

[28] F. Medina, Reducing metal alloy powder costs for use in powder bed fusion additive manufacturing: Improving the economics for production, 2013.

[29] X. Zhao, J. Chen, X. Lin, W. Huang, Study on microstructure and mechanical properties of laser rapid forming Inconel 718, Materials Science and Engineering: A 478(1) (2008) 119-124.

[30] H. Qi, M. Azer, A. Ritter, Studies of standard heat treatment effects on microstructure and mechanical properties of laser net shape manufactured Inconel 718, Metallurgical and Materials Transactions A 40(10) (2009) 2410-2422.

[31] C. Li, C. Fu, Y. Guo, F. Fang, Fast prediction and validation of part distortion in selective laser melting, Procedia Manufacturing 1 (2015) 355-365.

[32] A. Bauereiß, T. Scharowsky, C. Körner, Defect generation and propagation mechanism during additive manufacturing by selective beam melting, Journal of Materials Processing Technology 214(11) (2014) 2522-2528.

[33] Y. Li, D. Gu, Parametric analysis of thermal behavior during selective laser melting additive manufacturing of aluminum alloy powder, Materials & Design 63 (2014) 856-867.

[34] G. Strano, L. Hao, R.M. Everson, K.E. Evans, Surface roughness analysis, modelling and prediction in selective laser melting, Journal of Materials Processing Technology 213(4) (2013)

589-597.

[35] H. Gong, K. Rafi, H. Gu, T. Starr, B. Stucker, Analysis of defect generation in Ti–6Al–4V parts made using powder bed fusion additive manufacturing processes, Additive Manufacturing 1 (2014) 87-98.

[36] S.A. Khairallah, A. Anderson, Mesoscopic simulation model of selective laser melting of stainless steel powder, Journal of Materials Processing Technology 214(11) (2014) 2627-2636.

[37] L.N. Carter, M.M. Attallah, R.C. Reed, Laser powder bed fabrication of nickel-base superalloys: influence of parameters; characterisation, quantification and mitigation of cracking, Superalloys 2012 (2012) 577-586.

[38] K. Kempen, L. Thijs, B. Vrancken, S. Buls, J. Van Humbeeck, J. Kruth, Producing crack-free, high density M2 Hss parts by selective laser melting: pre-heating the baseplate, Proceedings of the 24th international solid freeform fabrication symposium. Laboratory for freeform fabrication, Austin, TX, 2013, pp. 131-139.

[39] J.-P. Kruth, L. Froyen, J. Van Vaerenbergh, P. Mercelis, M. Rombouts, B. Lauwers, Selective laser melting of iron-based powder, Journal of Materials Processing Technology 149(1) (2004) 616-622.

[40] P. Mercelis, J.-P. Kruth, Residual stresses in selective laser sintering and selective laser melting, Rapid Prototyping Journal 12(5) (2006) 254-265.

[41] T. Gnäupel-Herold, J. Slotwinski, S. Moylan, D.E. Chimenti, L.J. Bond, D.O. Thompson, Neutron measurements of stresses in a test artifact produced by laser-based additive manufacturing, AIP Conference Proceedings, AIP, 2014, pp. 1205-1212.

[42] P. Rangaswamy, T. Holden, R. Rogge, M. Griffith, Residual stresses in components formed by the laserengineered net shaping (LENS®) process, The Journal of strain analysis for engineering design 38(6) (2003) 519-527.

[43] L. Sochalski-Kolbus, E.A. Payzant, P.A. Cornwell, T.R. Watkins, S.S. Babu, R.R. Dehoff, M. Lorenz, O. Ovchinnikova, C. Duty, Comparison of residual stresses in Inconel 718 simple parts made by electron beam melting and direct laser metal sintering, Metallurgical and Materials Transactions A 46(3) (2015) 1419-1432.

[44] C.A. Brice, W.H. Hofmeister, Determination of bulk residual stresses in electron beam additive-manufactured aluminum, Metallurgical and Materials Transactions A 44(11) (2013) 5147-5153.

[45] A. Wu, M. LeBlanc, M. Kumar, G. Gallegos, D. Brown, W. King, Effect of laser scanning pattern and build direction in additive manufacturing on anisotropy, porosity and residual stress, 2014 TMS Annual Meeting & Exhibition, 2014.

[46] A.S. Wu, D.W. Brown, M. Kumar, G.F. Gallegos, W.E. King, An experimental investigation into additive manufacturing-induced residual stresses in 316L stainless steel, Metallurgical and Materials Transactions A 45(13) (2014) 6260-6270.

[47] N. Mostafa, H.M. Syed, S. Igor, G. Andrew, A study of melt flow analysis of an ABS-Iron composite in fused deposition modelling process, Tsinghua Science & Technology 14 (2009) 29-37.

[48] M. Masoomi, X. Gao, S.M. Thompson, N. Shamsaei, L. Bian, A. Elwany, Modeling, simulation and experimental validation of heat transfer during selective laser melting, ASME 2015 International Mechanical Engineering Congress and Exposition, American Society of Mechanical Engineers, 2015, pp. V02AT02A007-V02AT02A007.

[49] A. Gusarov, I. Yadroitsev, P. Bertrand, I. Smurov, Heat transfer modelling and stability analysis of selective laser melting, Applied Surface Science 254(4) (2007) 975-979.

[50] B. Song, S. Dong, H. Liao, C. Coddet, Process parameter selection for selective laser melting of Ti6Al4V based on temperature distribution simulation and experimental sintering, The International Journal of Advanced Manufacturing Technology 61(9) (2012) 967-974.

[51] R.B. Patil, V. Yadava, Finite element analysis of temperature distribution in single metallic powder layer during metal laser sintering, International Journal of Machine Tools and Manufacture 47(7) (2007) 1069-1080.

[52] J. Yin, H. Zhu, L. Ke, W. Lei, C. Dai, D. Zuo, Simulation of temperature distribution in single metallic powder layer for laser micro-sintering, Computational Materials Science 53(1) (2012) 333-339.

[53] A.K. Ibraheem, B. Derby, P.J. Withers, Thermal and residual stress modelling of the selective laser sintering process, DTIC Document, 2003.

[54] K. Zeng, D. Pal, B. Stucker, A review of thermal analysis methods in Laser Sintering and Selective Laser Melting, Proceedings of Solid Freeform Fabrication Symposium Austin, TX, 2012.

[55] Z. Jian, L. Deying, Z. Longzhi, Z. Mingjuan, Simulation of temperature field in selective laser sintering of copper powder, Mechanic Automation and Control Engineering (MACE), 2010 International Conference on, IEEE, 2010, pp. 3282-3285.

[56] L. Van Belle, G. Vansteenkiste, J.C. Boyer, Comparisons of numerical modelling of the Selective Laser Melting, Key Engineering Materials, Trans Tech Publ, 2012, pp. 1067-1072.

[57] E.R. Denlinger, J. Irwin, P. Michaleris, Thermomechanical modeling of additive manufacturing large parts, Journal of Manufacturing Science and Engineering 136(6) (2014) 061007.

[58] T.-M. Wang, J.-T. Xi, Y. Jin, A model research for prototype warp deformation in the FDM process, The International Journal of Advanced Manufacturing Technology 33(11-12) (2007) 1087-1096.

[59] J.L. Beuth, S. Narayan, Residual stress-driven delamination in deposited multi-layers, International Journal of Solids and Structures 33(1) (1996) 65-78.

[60] Y. Zhang, K. Chou, A parametric study of part distortions in fused deposition modelling using three-dimensional finite element analysis, Proceedings of the Institution of Mechanical Engineers, Part B: Journal of Engineering Manufacture 222(8) (2008) 959-968.

[61] Y. Zhang, Y. Chou, Three-dimensional finite element analysis simulations of the fused deposition modelling process, Proceedings of the Institution of Mechanical Engineers, Part B: Journal of Engineering Manufacture 220(10) (2006) 1663-1671.

[62] G. Bugeda, M. Cervera, G. Lombera, E. Onate, Numerical analysis of stereolithography processes using the finite element method, Rapid Prototyping Journal 1(2) (1995) 13-23.

[63] A. Nickel, D. Barnett, F. Prinz, Thermal stresses and deposition patterns in layered manufacturing, Materials Science and Engineering: A 317(1) (2001) 59-64.

[64] K. Dai, L. Shaw, Finite element analysis of the effect of volume shrinkage during laser densification, Acta materialia 53(18) (2005) 4743-4754.

[65] K. Dai, L. Shaw, Thermal and mechanical finite element modeling of laser forming from metal and ceramic powders, Acta Materialia 52(1) (2004) 69-80.

[66] K. Dai, L. Shaw, Thermal and stress modeling of multi-material laser processing, Acta

Materialia 49(20) (2001) 4171-4181.

[67] S. Kumar, Selective laser sintering: a qualitative and objective approach, JOM Journal of the Minerals, Metals and Materials Society 55(10) (2003) 43-47.

[68] J. Goldak, A. Chakravarti, M. Bibby, A new finite element model for welding heat sources, Metallurgical and Materials Transactions B 15(2) (1984) 299-305.

[69] S.M. Thompson, L. Bian, N. Shamsaei, A. Yadollahi, An overview of Direct Laser Deposition for additive manufacturing; Part I: Transport phenomena, modeling and diagnostics, Additive Manufacturing 8 (2015) 36-62.

[70] T. Chen, Y. Zhang, Numerical simulation of two-dimensional melting and resolidification of a two-component metal powder layer in selective laser sintering process, Numerical Heat Transfer, Part A: Applications 46(7) (2004) 633-649.

[71] A. Vasinonta, J.L. Beuth, M.L. Griffith, Process maps for controlling residual stress and melt pool size in laser-based SFF processes, Solid Freeform Fabrication Proceedings, Proc. 2000 Solid Freeform Fabrication Symposium, Austin, 2000, p. 206.

[72] Z. Fan, F. Liou, Numerical modeling of the additive manufacturing (AM) processes of titanium alloy, Titanium Alloys-Towards Achieving Enhanced Properties for Diversified Applications, InTech2012.

[73] Q. Wang, J. Li, M. Gouge, A.R. Nassar, P.P. Michaleris, E.W. Reutzel, Physics-Based Multivariable Modeling and Feedback Linearization Control of Melt-Pool Geometry and Temperature in Directed Energy Deposition, Journal of Manufacturing Science and Engineering 139(2) (2017) 021013.

[74] C. Körner, E. Attar, P. Heinl, Mesoscopic simulation of selective beam melting processes, Journal of Materials Processing Technology 211(6) (2011) 978-987.

[75] L.-Q. Chen, Phase-field models for microstructure evolution, Annual review of materials research 32(1) (2002) 113-140.

[76] B.S. Fromm, K. Chang, D.L. McDowell, L.-Q. Chen, H. Garmestani, Linking phase-field and finite-element modeling for process–structure–property relations of a Ni-base superalloy, Acta Materialia 60(17) (2012) 5984-5999.

[77] T. Craeghs, F. Bechmann, S. Berumen, J.-P. Kruth, Feedback control of Layerwise Laser Melting using optical sensors, Physics Procedia 5 (2010) 505-514.

[78] T. Craeghs, S. Clijsters, E. Yasa, F. Bechmann, S. Berumen, J.-P. Kruth, Determination of geometrical factors in Layerwise Laser Melting using optical process monitoring, Optics and Lasers in Engineering 49(12) (2011) 1440-1446.

[79] S. Berumen, F. Bechmann, S. Lindner, J.-P. Kruth, T. Craeghs, Quality control of laser-and powder bed-based Additive Manufacturing (AM) technologies, Physics procedia 5 (2010) 617-622.

[80] J.-P. Kruth, J. Duflou, P. Mercelis, J. Van Vaerenbergh, T. Craeghs, J. De Keuster, On-line monitoring and process control in selective laser melting and laser cutting, Proceedings of the 5th Lane Conference, Laser Assisted Net Shape Engineering, 2007, pp. 23-37.

[81] P. Lott, H. Schleifenbaum, W. Meiners, K. Wissenbach, C. Hinke, J. Bültmann, Design of an optical system for the in situ process monitoring of selective laser melting (SLM), Physics Procedia 12 (2011) 683-690.

[82] S. Clijsters, T. Craeghs, S. Buls, K. Kempen, J.-P. Kruth, In situ quality control of the selective

laser melting process using a high-speed, real-time melt pool monitoring system, The International Journal of Advanced Manufacturing Technology 75(5-8) (2014) 1089-1101.

[83] M. Golzar, R. Beyreuther, H. Brünig, B. Tändler, R. Vogel, Online temperature measurement and simultaneous diameter estimation of fibers by thermography of the spinline in the melt spinning process, Advances in Polymer Technology 23(3) (2004) 176-185.

[84] V.T. Marla, R.L. Shambaugh, D.V. Papavassiliou, Use of an infrared camera for accurate determination of the temperature of polymer filaments, Industrial & Engineering Chemistry Research 46(1) (2007) 336-344.

[85] V.T. Marla, R.L. Shambaugh, D.V. Papavassiliou, Online measurement of fiber diameter and temperature in the melt-spinning and melt-blowing processes, Industrial & Engineering Chemistry Research 48(18) (2009) 8736-8744.

[86] K.B. Migler, A.J. Bur, Fluorescence based measurement of temperature profiles during polymer processing, Polymer Engineering & Science 38(1) (1998) 213-221.

[87] A.J. Bur, S.C. Roth, M.A. Spalding, D.W. Baugh, K.A. Koppi, W.C. Buzanowski, Temperature gradients in the channels of a single-screw extruder, Polymer Engineering & Science 44(11) (2004) 2148-2157.

[88] P.K. Rao, J.P. Liu, D. Roberson, Z.J. Kong, C. Williams, Online real-time quality monitoring in additive manufacturing processes using heterogeneous sensors, Journal of Manufacturing Science and Engineering 137(6) (2015) 061007.

[89] Q. Sun, G.M. Rizvi, C.T. Bellehumeur, P. Gu, Effect of processing conditions on the bonding quality of FDM polymer filaments, Rapid Prototyping Journal 14(2) (2008) 72-80.

[90] M.D. Monzón, I. Gibson, A.N. Benítez, L. Lorenzo, P.M. Hernández, M.D. Marrero, Process and material behavior modeling for a new design of micro-additive fused deposition, The International Journal of Advanced Manufacturing Technology 67(9) (2013) 2717-2726.

[91] R.B. Dinwiddie, L.J. Love, J.C. Rowe, Real-time process monitoring and temperature mapping of a 3D polymer printing process, 2013, pp. 87050L-87050L-9.

[92] J.E. Seppala, K.D. Migler, Infrared thermography of welding zones produced by polymer extrusion additive manufacturing, Additive Manufacturing 12, Part A (2016) 71-76.

[93] G. Tapia, A. Elwany, A review on process monitoring and control in metal-based additive manufacturing, Journal of Manufacturing Science and Engineering 136(6) (2014) 060801.

[94] W.H. Peter, Proximity sensor, Google Patents, 1998.

[95] R. Anitha, S. Arunachalam, P. Radhakrishnan, Critical parameters influencing the quality of prototypes in fused deposition modelling, Journal of Materials Processing Technology 118(1) (2001) 385-388.

[96] T. Nancharaiah, D.R. Raju, V.R. Raju, An experimental investigation on surface quality and dimensional accuracy of FDM components, International Journal on Emerging Technologies 1(2) (2010) 106-111.

[97] K. Thrimurthulu, P.M. Pandey, N.V. Reddy, Optimum part deposition orientation in fused deposition modeling, International Journal of Machine Tools and Manufacture 44(6) (2004) 585-594.

[98] D. Horvath, R. Noorani, M. Mendelson, Improvement of surface roughness on ABS 400 polymer using design of experiments (DOE), Materials Science Forum, Trans Tech Publ, 2007, pp. 2389-2392.

[99] C. Chung Wang, T.-W. Lin, S.-S. Hu, Optimizing the rapid prototyping process by integrating the Taguchi method with the Gray relational analysis, Rapid Prototyping Journal 13(5) (2007) 304-315.

[100] A.K. Sood, R. Ohdar, S. Mahapatra, Improving dimensional accuracy of fused deposition modelling processed part using grey Taguchi method, Materials & Design 30(10) (2009) 4243-4252.

[101] R. Bansal, Improving dimensional accuracy of fused deposition modelling (FDM) parts using response surface methodology, National Institute of Technology Rourkela, 2011.

[102] S. Conti, J.P. Gosling, J.E. Oakley, A. O'hagan, Gaussian process emulation of dynamic computer codes, Biometrika (2009) asp028.

[103] S. Conti, A. O'Hagan, Bayesian emulation of complex multi-output and dynamic computer models, Journal of statistical planning and inference 140(3) (2010) 640-651.

[104] J. Sjöberg, Q. Zhang, L. Ljung, A. Benveniste, B. Delyon, P.-Y. Glorennec, H. Hjalmarsson, A. Juditsky, Nonlinear black-box modeling in system identification: a unified overview, Automatica 31(12) (1995) 1691-1724.

[105] J. Sacks, W.J. Welch, T.J. Mitchell, H.P. Wynn, Design and analysis of computer experiments, Statistical science (1989) 409-423.

[106] M. Bayarri, J. Berger, J. Cafeo, G. Garcia-Donato, F. Liu, J. Palomo, R. Parthasarathy, R. Paulo, J. Sacks, D. Walsh, Computer model validation with functional output, The Annals of Statistics (2007) 1874-1906.

[107] J.O. Ramsay, Functional data analysis, Wiley Online Library2006.

[108] D. Higdon, J. Gattiker, B. Williams, M. Rightley, Computer model calibration using high-dimensional output, Journal of the American Statistical Association 103(482) (2008) 570-583.

[109] K.-T. Fang, R. Li, A. Sudjianto, Design and modeling for computer experiments, CRC Press2005.

[110] F. Liu, M. West, A dynamic modelling strategy for Bayesian computer model emulation, Bayesian Analysis 4(2) (2009) 393-411.

[111] B. Williams, D. Higdon, J. Gattiker, L. Moore, M. McKay, S. Keller-McNulty, Combining experimental data and computer simulations, with an application to flyer plate experiments, Bayesian Analysis 1(4) (2006) 765-792.

[112] J. Rougier, Efficient emulators for multivariate deterministic functions, Journal of Computational and Graphical Statistics 17(4) (2008) 827-843.

[113] Y. Hung, V.R. Joseph, S.N. Melkote, Analysis of computer experiments with functional response, Technometrics 57(1) (2015) 35-44.

[114] D. Higdon, M. Kennedy, J.C. Cavendish, J.A. Cafeo, R.D. Ryne, Combining field data and computer simulations for calibration and prediction, SIAM Journal on Scientific Computing 26(2) (2004) 448-466.

[115] P.Z. Qian, C.J. Wu, Bayesian hierarchical modeling for integrating low-accuracy and high-accuracy experiments, Technometrics 50(2) (2008) 192-204.

[116] S. Wang, W. Chen, K.-L. Tsui, Bayesian validation of computer models, Technometrics 51(4) (2009) 439-451.

[117] A. Cooke, J. Soons, Variability in the geometric accuracy of additively manufactured test

parts, 21st annual international solid freeform fabrication symposium, Austin, Texas, USA, 2010, pp. 1-12.

[118] M. Atif Yardimci, S. Güçeri, Conceptual framework for the thermal process modelling of fused deposition, Rapid Prototyping Journal 2(2) (1996) 26-31.

[119] H. Ramanath, C. Chua, K. Leong, K. Shah, Melt flow behaviour of poly-ε-caprolactone in fused deposition modelling, Journal of Materials Science: Materials in Medicine 19(7) (2008) 2541-2550.

[120] L.B. Ji, T.R. Zhou, Finite element simulation of temperature field in fused deposition modeling, Advanced Materials Research, Trans Tech Publ, 2010, pp. 2585-2588.

[121] Y. Dutil, D.R. Rousse, N.B. Salah, S. Lassue, L. Zalewski, A review on phase-change materials: mathematical modeling and simulations, Renewable and sustainable Energy reviews 15(1) (2011) 112-130.

[122] R.H. Nochetto, M. Paolini, C. Verdi, An Adaptive Finite Element Method for Two-Phase Stefan Problems in Two Space Dimensions. II: Implementation and Numerical Experiments, SIAM journal on scientific and statistical computing 12(5) (1991) 1207-1244.

[123] N. Provatas, N. Goldenfeld, J. Dantzig, Efficient computation of dendritic microstructures using adaptive mesh refinement, Physical Review Letters 80(15) (1998) 3308.

[124] N. Provatas, N. Goldenfeld, J. Dantzig, Adaptive mesh refinement computation of solidification microstructures using dynamic data structures, Journal of Computational Physics 148(1) (1999) 265-290.

[125] M. Ainsworth, J.T. Oden, A posteriori error estimation in finite element analysis, John Wiley & Sons2011.

[126] H. Conrad, T. Klose, T. Sandner, D. Jung, H. Schenk, H. Lakner, Modeling the Thermally Induced Curvature of Multilayer Coatings with COMSOL MultiphysicsTM, Proceedings of COMSOL Conference, 2008.

[127] I. Gibson, D.W. Rosen, B. Stucker, Additive manufacturing technologies, Springer2010.

[128] J.A. Brydson, Plastics materials, Butterworth-Heinemann1999.

[129] T. Tabi, I. Sajó, F. Szabó, A. Luyt, J. Kovács, Crystalline structure of annealed polylactic acid and its relation to processing, Express Polym Lett 4(10) (2010) 659-668.

[130] R. Winterton, Newton's law of cooling, Contemporary Physics 40(3) (1999) 205-212.

[131] J. Luttinen, A. Ilin, Efficient Gaussian Process Inference for Short-Scale Spatio-Temporal Modeling, AISTATS, 2012, pp. 741-750.

[132] T.J. Santner, B.J. Williams, W.I. Notz, The design and analysis of computer experiments, Springer Science & Business Media2013.

[133] A. Rosenfeld, A. Kak, Digital picture processing, Acad, Press, San Diego (1982).

[134] P.Z. Qian, B. Tang, C.J. Wu, Nested space-filling designs for computer experiments with two levels of accuracy, Statistica Sinica (2009) 287-300.

[135] R. Gonzalez, P. Wintz, Digital image processing, (1977).

[136] N. Bourbakis, C. Alexopoulos, Picture data encryption using scan patterns, Pattern Recognition 25(6) (1992) 567-581.

[137] C. De Boor, C. De Boor, E.-U. Mathématicien, C. De Boor, C. De Boor, A practical guide to

splines, Springer-Verlag New York1978.

[138] T. Mills, Time series techniques for economistscambridge university press, Cambridge et al 52 (1990) 68.

[139] B. Tang, Orthogonal array-based Latin hypercubes, Journal of the American statistical association 88(424) (1993) 1392-1397.

[140] J. Vlachopoulos, D. Strutt, Basic heat transfer and some applications in polymer processing, Plastics Technician's Toolbox 2 (2002) 21-33.

[141] I.A. Roberts, C. Wang, R. Esterlein, M. Stanford, D. Mynors, A three-dimensional finite element analysis of the temperature field during laser melting of metal powders in additive layer manufacturing, International Journal of Machine Tools and Manufacture 49(12) (2009) 916-923.

[142] P. Fischer, M. Locher, V. Romano, H.-P. Weber, S. Kolossov, R. Glardon, Temperature measurements during selective laser sintering of titanium powder, International Journal of Machine Tools and Manufacture 44(12) (2004) 1293-1296.

[143] T. Zhang, C.Y. Suen, A fast parallel algorithm for thinning digital patterns, Communications of the ACM 27(3) (1984) 236-239.

[144] C.-C. Cheng, G.-J. Peng, W.-L. Hwang, Subband weighting with pixel connectivity for 3-D wavelet coding, IEEE Transactions on Image Processing 18(1) (2009) 52-62.

Appendices

A. Neighborhood time difference

In computer graphics area, pixel connectivity [133] is a common approach to relate the pixels in two dimensional (2D) images to their neighbors. 8-connected pixels, similar with the concept called "Moore neighborhood" in cellular automata, are neighbors to every pixel that touches one of their edges or corners [143]. Besides the 4-connected pixels that touch one edge of the central pixel horizontally or vertically, the pixels with coordinates $(x \pm 1, y \pm 1)$ are also connected to the central pixel at (x, y) diagonally [144]. The concept of NTD is proposed to index the specific time location along the printing path on a printed layer. As shown in Figure 21, there are in total 25 elements in the interested region, where the arrow shows the printing pattern of the 3D printer. The number index inside every pixel indicates the extrusion sequence, which can be regarded as the functional space t as mentioned in previously. Here, I take pixel 13 (indicated as dark gray in Figure 21) as the interested pixel to illustrate how to calculate its NTD.

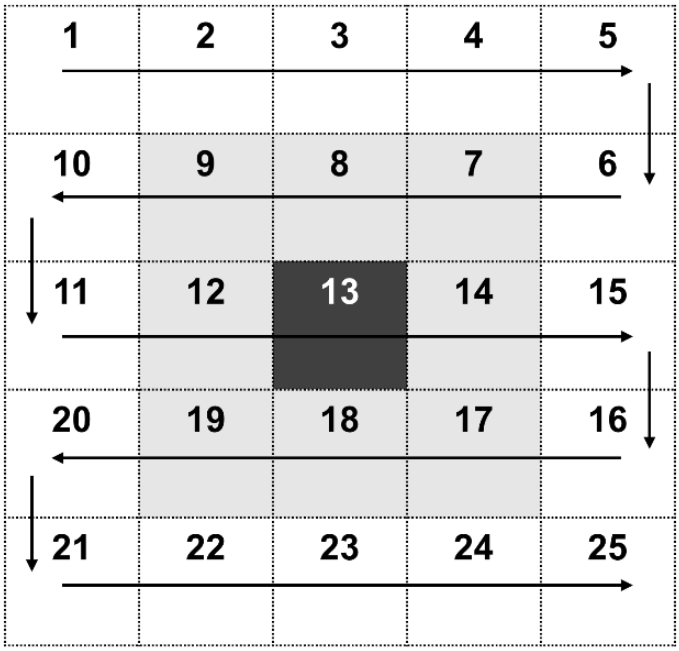

Figure 21. “Neighborhood time difference” illustration.

There are eight pixels 7-9, 12, 14, 17-19 (indicated as shallow gray in Figure 21) connected with pixel 13 based on the “8-connected pixels” rule. The NTD can be calculated by:

$$\boldsymbol{NTD} = \frac{\sum_{i=1}^{8}|t_i - t_0|}{8},$$

where t_i $(i = 1, \dots, 8)$ means the time index of the 8 neighborhood pixels and t_0 is the time index of the central pixel.

By substituting the time indexes of the 8-connected pixels of pixel 13 into the above equation, it can be obtained as:

$$NTD_{13} = \frac{(|7-13|+|8-13|+|9-13|+|12-13|+|14-13|+|17-13|+|18-13|+|19-13|)}{8} = 4.$$

B. Sensitivity Analysis of the Surrogate Model

The sensitivity analysis of the surrogate model is conducted for the two calibration parameters as illustrated in Figure 22. By fixing one calibration parameter to 0.5, the prediction results may vary with the other calibration parameter. The calibration parameters are evaluated at 11 separate values, resulting in 11 curves in Figure 22 (a) and (b), respectively. Changes of the calibration parameters are shown to significantly influence the model output, which suggests a successful construction of the surrogate model.

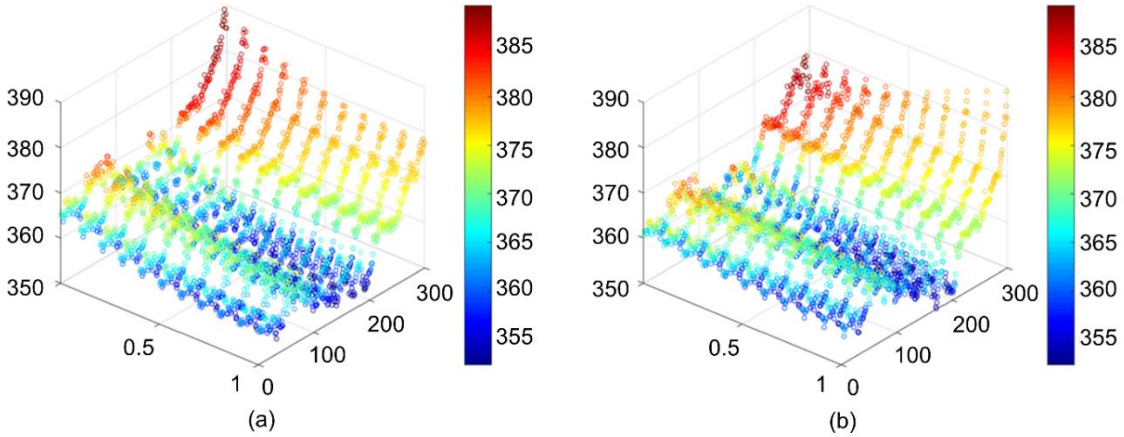

Figure 22. Sensitivity study of the surrogate model (a) for η_1; (b) for η_2 (unit: K).